COMPARISON OF NONLINEAR FILTERS

FOR AN AUTONOMOUS LUNAR MISSION

USING EXISTING NAVIGATION TECHNIQUES

by

MATTHEW DAVID SHAVER

THESIS

Submitted in partial fulfillment of the requirements

for the degree of Master of Science in Aerospace Engineering at

The University of Texas at Arlington

May, 2018

Supervising Committee:

Kamesh Subbarao, Supervising Professor
Alan Bowling
Donald Wilson

DEDICATION

I would like to dedicate this thesis first and foremost to my wonderful wife who kept our family working during my research work.  I could never have done this without you.  I want to further dedicate this work to my son and daughter so that they know hard work and knowledge will bring a brighter future to those who aspire.

May 7, 2018

# ACKNOWLEDGEMENTS

I would like to take the opportunity to thank all of those who have guided, inspired and helped me with my academic growth.  This thesis is a testament to what one can do if given the opportunity.

I would like to thank my advising professor, Dr. Kamesh Subbarao, for advice and guidance through this process to help me achieve my dream of obtaining a Master's degree.

Also, I would like to thank my thesis committee members, Dr. Alan Bowling and Dr. Don Wilson, for providing their time and knowledge to help me with my work.

<div align="right">May 7, 2018</div>

LIST OF ILLUSTRATIONS

## LIST OF TABLES

ABSTRACT


COMPARISON OF NONLINEAR FILTERS

FOR AN AUTONOMOUS LUNAR MISSION

USING EXISTING NAVIGATION TECHNIQUES



Matthew David Shaver, MS


The University of Texas at Arlington, 2018


Supervising Professor: Kamesh Subbarao

Navigation systems play an important role for autonomous spacecraft.  Earth based navigation systems such as GPS provide accurate positioning for orbiting spacecraft.  In the case of lunar orbit, GPS is not available so other navigation techniques have to be used.  This thesis proposes a novel idea to use Laser Ranging Retroreflectors, placed on the Moon's surface during the Apollo program, as a means of providing position information to an orbiting autonomous spacecraft.  An Inertial Navigation System consisting of fusion of LRRR position data and Inertial Measurement Unit providing gyro and accelerometer data will be utilized during orbit about the Moon. Prior arriving in a lunar orbit, celestial navigation using the stars will provide positioning information as the vehicle translates along a lunar intercept path.  The entire lunar operational profile will be evaluated using nonlinear filter techniques (Extended Kalman Filter and Unscented Kalman Filter).  Trade-offs between filter accuracy, computational cost and ease of implementation will be assessed.

TABLE OF CONTENTS

CHAPTER 1

MOTIVATION

Spacecraft navigation about the Moon is limited to a few options for obtaining tracking data.  The Deep Space Network (DSN) has the capability to provide this service only if a vehicle has line of sight to the radar sites.  This service is highly utilized by the space community that perform interplanetary operations.  As a consequence, the amount of time a vehicle can use this service is limited to perform vehicle tracking as well as availability.  Due to the DSN scheduling constraints, proposals have been made including use of lunar satellites to provide service to vehicles in lunar orbit.  Since lunar tracking and communication satellites are not in existence, other means of positioning data were investigated to perform navigation.  This thesis proposes another way to provide positioning data to a spacecraft using available tracking sources.

For this analysis, the vehicle's trajectory will be analyzed in two parts, cislunar and lunar orbit. Cislunar navigation estimation will utilize celestial navigation techniques to determine position and velocity.  Star trackers data will provide position measurements to the filters for calculation of the estimated state of the vehicle.   Once the vehicle is in lunar orbit, the filters will incorporate gyro and accelerometer data along with Lidar-based laser ranging measurements reflected from Laser Ranging Retro-Reflectors (LRRR) arrays located on the Moon's surface.  These LRRRs were placed on the lunar surface during lunar surface operations of the Apollo program.  They are still in use today providing Earth-based laser ranging of the Moon.  The Lidar measurements will be analogous to measurements from ground-based tracking sites on the Earth providing range, azimuth and elevation information.  This type of Lidar application using LRRRs is a novel approach to providing tracking data for a vehicle in orbit.  Lidars have been used for mapping of the Earth's surface and can be modified to provide the tracking data

analyzed in this thesis.  Also, Lidar data fused with an Integrated Navigation System (INS) has been previously investigated as an alternative option to a GPS/INS system where GPS is not available [12].

This thesis will investigate nonlinear Kalman filtering techniques to process the proposed tracking data and compare them to each other.  The accuracy of the estimated state is based on how precise sensors can measure and how well the system dynamics are modeled. The most common filter is the Extended Kalman Filter (EKF).  It is used extensively in spacecraft navigation systems because of its ease of computation through linearization of error and its computational speed.  This was advantageous when memory space and processing speed was at a premium during the 1960's.  The processing power and memory of today's computers have vastly increased, which allows for other types of filter applications.  Coinciding with processing speed, computer architecture has evolved to include parallel processing.  This is advantageous for reducing computation time for nonlinear filter applications.

Advances in filtering have provided other means of estimating more precise navigation states over the EKF by using other methods.  For this analysis, another nonlinear filter called the Unscented Kalman Filter (UKF) will be compared to the EKF. Comparisons in the form of accuracy and convergence will be investigated as well as the computational speed.  The UKF provides more accurate initial estimates given a small amount of data compared to the EKF.  This type of filter propagates a number of sigma points through a time step which will increase processing time.  This processing is more straightforward than the EKF which needs to calculate partial derivatives.  Computational speed is sacrificed for accuracy and will factor into determining whether this is an acceptable method.

CHAPTER 2

NAVIGATION TECHNIQUES


History

First published by Dr. Rudoplh Kalman in 1960 [1], the Kalman filter was designed for linear systems with continuous measurements.  A nonlinear system with discrete time measurements was needed for lunar navigation for the Apollo program.  A modified version of the Kalman filter was developed called the extended Kalman filter (EKF) [2].  This modified filter constructed a linear system about the estimate of the state.  The linear system provided an accurate navigation estimate of the truth state while keeping computations and memory allocations at a minimum.  This allowed Apollo program to be able to navigate to the moon [3].  Since then other methods of filtering have been created to make it more accurate and efficient.  The Unscented Kalman Filter and Particle Filter are two nonlinear filters that have been developed to estimate nonlinear systems.  These types of filters will be used for the analysis in this thesis.


Vehicle Trajectory

The trajectory will start after the vehicle performs a Trans-Lunar Injection (TLI) burn on an intercept course with the Moon.  A patched conic will be used to calculate a hyperbolic trajectory for lunar approach [8].  Assuming a burn targeted minimum approach distance, the vehicle will be placed in a 315 x 200 km orbit (170 x 108 nmi) for 2 orbits.  The orbit will be circularized to 200 x 200 km (108 x 108 nmi).  The vehicle will orbit the Moon twice when the simulation ends. This type of lunar insertion and orbit scheme is similar to Apollo missions. The altitude of the orbit is higher than the Apollo

mission to allow the vehicle line of sight to the retro reflector arrays located on the lunar surface.  These arrays will be used for ranging measurements discussed later.

Celestial Navigation

Celestial navigation is a method of determining position [7,13,14].  The method involves the use line of sight angle measurements from two known celestial objects, measuring planetary object angular diameter, observing star occultation by an object, or radar measurements. For this analysis, two of the four types of measurements will be utilized.

Line of sight angle measurements between a star and a planetary object will be taken at specific intervals during cislunar travel.  The planetary objects will be either the Earth or the Moon dependent upon distance to the object.  Also, the observed angular diameter of either the Earth or Moon will be used to provide a measured range value that will be included in the position determination from the angle measurements.  The position of the vehicle can be determined by taking measurements from these two sources.  In order to make the system observable the combination of angle measurements, star-planet, star-planet, and planet-diameter were used.  The two star-planet angles provide the foundation for obtaining a navigation fix.  The angle sets the vehicle's position on the surface of a cone with its apex at the planet's centroid and its axis parallel to the vehicle's line of sight.  The second star-planet provides another cone with its own apex and axis. The intersection of the two cones create two straight lines with one being the line of position of the vehicle.  If a third star-planet angle were taken, it would confirm the two lines.  However, there may be difficulty in determining the correct one and can result in an unobservable system.  Including the angular diameter measurement provides the radial distance of the vehicle from the planet and establishes the position fix along the

4

line of position obtained from the two star-planet measurements above.  A navigation fix can be obtained with this method.  The more orthogonal the line of sight vectors are to the stars the more accurate the position.  Therefore, star selection for taking measurements factor into position estimation.

## Optical Measurements

The vehicle will use star trackers to obtain measurements using line of sight of stars using known locations of those stars.  As stated earlier, the star tracker will observe the angle between a star and planetary object.  Figure 2-1 shows the relative geometry of the stars, planet ($P_0$) and vehicle ($S_0$).  Due to the timing of when the measurements are taken along the cislunar trajectory, the Earth will be used as the reference body.  Similar to Apollo missions, the star sighting measurements will be taken around six hours and twenty-four hours after the TLI burn to provide an update to the trajectory prior to planned midcourse correction burns referred to as MC1 and MC2.  These measurement periods will also be referred to as MC1 and MC2 in the analysis since they take place before the burns.
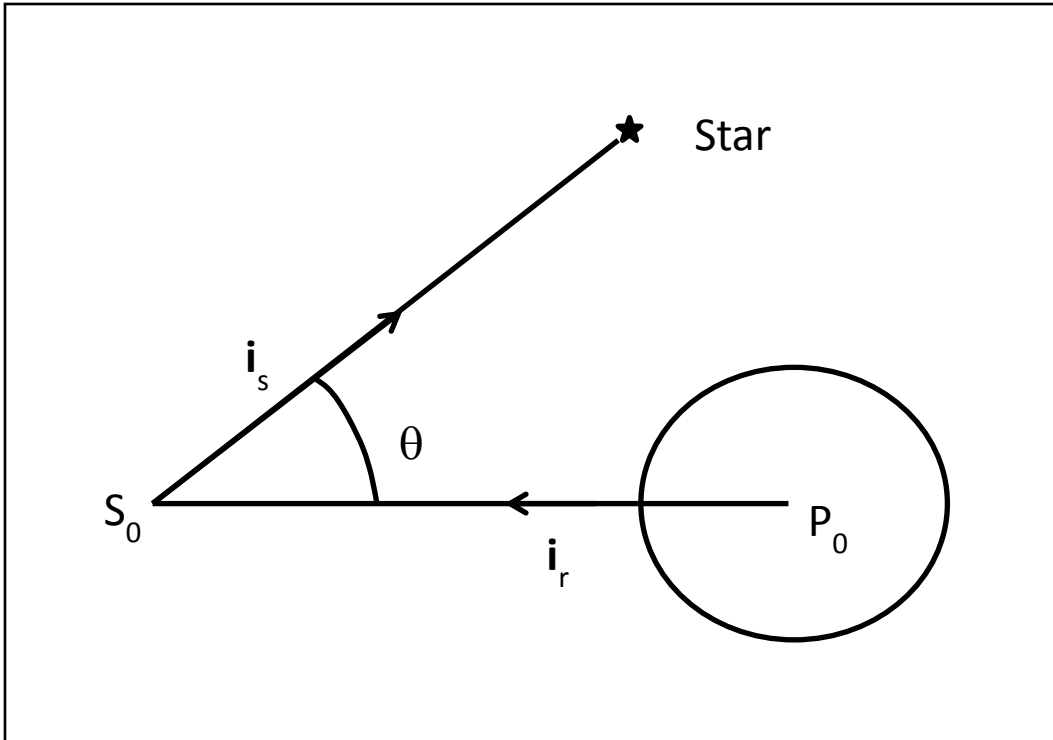
Figure 2-1 Star-Planet Angle Geometry

From Figure 2-1, the relationship between the observable and vehicle position is taken by the dot product of the two vectors if the form

$$\cos\theta = \frac{\boldsymbol{R}\cdot\boldsymbol{i}_s}{r} \tag{3.1}$$

where $\theta$ is the observed angle measurement, $\boldsymbol{R}$ is the vector of spacecraft relative to the planetary body, $r$ is the radial distance to the planet, and $\boldsymbol{i}_s$ is the unit vector in the direction of the star. Due to the distance of stars, their directions are assumed to be fixed and independent of any observation. *The Astronomical Almanac*, a yearly publication provided by the US Navy [11], provides star locations in sidereal hour angle ($\lambda$) and declination ($\phi$). The unit vector of the star can be determined by transforming the spherical direction to Cartesian direction

$$\boldsymbol{i}_s = \frac{1}{r} \begin{bmatrix} \cos \varphi \cos \lambda \\ \cos \varphi \sin \lambda \\ \sin \varphi \end{bmatrix} \qquad (2.2)$$

The derivative of the angle $\theta$ with respect to the position state also known as the measurement geometry vector is

$$\boldsymbol{h} = \frac{1}{r \sin \theta} (\cos \theta \, \boldsymbol{i}_r + \boldsymbol{i}_s) \qquad (2.3)$$

with $i_r$ being the unit vector of the vehicle relative to the planet. Next, using Figure 3-2, the measured angular diameter of a planet is found from

$$r \sin \frac{1}{2} \theta = \frac{1}{2} D \qquad (2.4)$$

where $\theta$ is the observed angular diameter, $r$ is the radial distance from the planet, and $D$ is the actual diameter of the planet. The measurement geometry vector is derived to be

$$\boldsymbol{h} = -\frac{D}{r^2 \cos \frac{1}{2} \theta} \boldsymbol{i}_r \qquad (2.5)$$
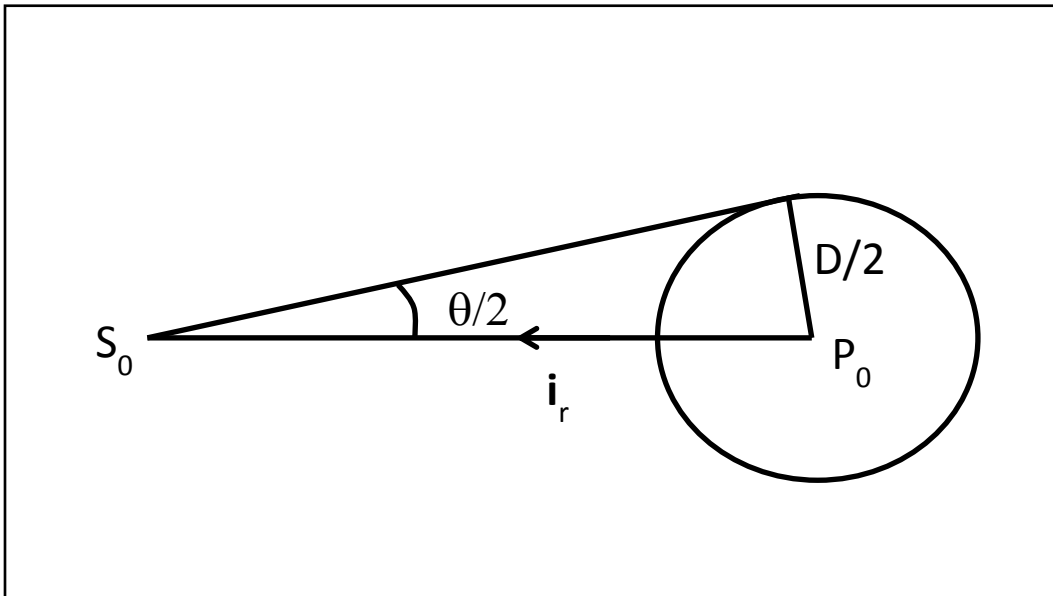


Figure 2-2 Angular Diameter of Planet

A 3x3 measurement geometry matrix, $\boldsymbol{H}$, is formed by taking the above transformation from a star-planet, star-planet, angular diameter combination.

$$\boldsymbol{H} = \begin{bmatrix} \dfrac{1}{r \sin \theta_{s1}} (\cos \theta \, \boldsymbol{i}_r^T + \boldsymbol{i}_{s1}^T) \\[2mm] \dfrac{1}{r \sin \theta_{s2}} (\cos \theta \, \boldsymbol{i}_r^T + \boldsymbol{i}_{s2}^T) \\[2mm] -\dfrac{D}{r^2 \cos \frac{1}{2} \theta_3} \boldsymbol{i}_r^T \end{bmatrix} \qquad (2.6)$$

### Lunar Orbit Navigation

Orbit navigation about the Moon will consist of estimating attitude, position and velocity. This will be accomplished using laser ranging observations with IMU input forming an INS. An IMU will provide gyro and accelerometer data to incorporate into the attitude and translation motion respectively. A Lidar onboard the spacecraft and will measure the time of reflected light to the sensor using Lunar Ranging Retro-Reflector (LRRR) arrays located on the lunar surface. These LRRRs were placed on the surface of the Moon during Apollo missions (11, 14 and 15) and have been used extensively for determining the range of the Moon from the Earth through the Lunar Ranging Experiment. This analysis will assume the Lidar will provide range, azimuth and elevation measurement that will be incorporated as position into the filters. The vehicle will maintain a constant angular rate in order to keep the Lidar onboard the vehicle pointed at the LRRR as it passes over the array. This angular rate along with sensed accelerations will be fed into the navigation state estimate.

Integrated Navigation System

The measurement model of the IMU provides accelerometer and gyro sensors [5]. There will be three gyros and accelerometers. Each single axis sensor will be aligned with the body axes of the vehicle. The gyro rate model for a single axis is given as

$$\widetilde{\boldsymbol{\omega}}_{B/I}^{B} = \boldsymbol{\omega}_{B/I}^{B} + \boldsymbol{\beta}_g + \boldsymbol{\eta}_{gv} \tag{2.7}$$

$$\dot{\boldsymbol{\beta}}_g = \boldsymbol{\eta}_{gu} \tag{2.8}$$

where $\beta_g$ is the gyro bias and $\eta_{gv}$ and $\eta_{gu}$ are zero mean Gaussian white noise processes. The superscript indicates the reference frame: B for body frame, I for inertial frame, or N for navigation frame. The subscript indicates the relation. In this case, the angular rate relative to B (body) frame/expressed in I (inertial) coordinates.

The accelerometer is similar to the gyro model

$$\widetilde{\boldsymbol{a}}^{B} = \boldsymbol{a}^{B} + \boldsymbol{\beta}_a + \boldsymbol{\eta}_{av} \tag{2.9}$$

$$\dot{\boldsymbol{\beta}}_a = \boldsymbol{\eta}_{au} \tag{2.10}$$

In addition to IMU data the navigation system will receive range and bearing measurements from a Lidar onboard the spacecraft that receives reflected light from LRRR arrays on the lunar surface. Measurements will be given in azimuth, elevation and range for a given LRRR location.

The integrated navigation system estimates attitude, position and velocity as well as biases for the accelerometers and gyros. The attitude will be represented by the quaternion, $\boldsymbol{q}$. The quaternion is a four-dimensional vector defined as

$$\boldsymbol{q} = \begin{bmatrix} \boldsymbol{\varrho} \\ q_4 \end{bmatrix} \tag{2.11}$$

where $\boldsymbol{\varrho}$ is the vector part and $q_4$ is the scalar part. Use of the quaternion is advantageous as it does not have singularities versus other means of attitude

representations such as Euler angles or Modified Rodrigues Parameters. Successive

rotations of a quaternion are achieved through quaternion multiplication. The attitude

quaternion kinematics equation is

$$\dot{\hat{q}} = \frac{1}{2}\Omega(\hat{\boldsymbol{\omega}}_{B/N}^B)\hat{q} \tag{2.12}$$

$$\hat{\boldsymbol{\omega}}_{B/N}^B = \tilde{\boldsymbol{\omega}}_{B/I}^B - \hat{\boldsymbol{\beta}}_g - A_N^B(\hat{q})\hat{\boldsymbol{\omega}}_{N/I}^N \tag{2.13}$$

$$\hat{\boldsymbol{\omega}}_{N/I}^N = \omega_m \begin{bmatrix} \cos\hat{\phi} \\ 0 \\ -\sin\hat{\phi} \end{bmatrix} + \begin{bmatrix} \dfrac{\hat{v}_E}{\hat{R}_m} \\ \dfrac{\hat{v}_N}{\hat{R}_m} \\ -\dfrac{\hat{v}_E \tan\hat{\phi}}{\hat{R}_m} \end{bmatrix} \tag{2.14}$$

where

$$\Omega(\omega) = \begin{bmatrix} -[\omega \times] & \omega \\ -\omega^T & 0 \end{bmatrix} \tag{2.15}$$

and the attitude matrix is defined as

$$A(\boldsymbol{q}) = \Xi^T(\boldsymbol{q})\Psi(\boldsymbol{q}) \tag{2.16}$$

$$\Xi(\boldsymbol{q}) = \begin{bmatrix} q_4 I_{3\times3} + [\boldsymbol{\varrho} \times] \\ -\boldsymbol{\varrho}^T \end{bmatrix} \tag{2.17}$$

$$\Psi(\boldsymbol{q}) = \begin{bmatrix} q_4 I_{3\times3} - [\boldsymbol{\varrho} \times] \\ -\boldsymbol{\varrho}^T \end{bmatrix} \tag{2.18}$$

The attitude matrix, A, subscript indicates the "rotation from" frame and the

superscript indicates the "rotation to" frame. The parameter $\boldsymbol{\omega}_m$ is rotation rate of the

Moon.

Estimating a quaternion using the UKF presents a problem with dimensions. The

four-dimensional quaternion needs to be represented as a three dimensional component

vector. Using a version of the generalized Rodrigues parameters [9] can solve this issue

where the local error quaternion, $\delta\boldsymbol{q} = [\delta\boldsymbol{\varrho}^T \; \delta q_4]^T$ can be represented as

$$\delta \boldsymbol{p} \equiv f \frac{\delta \boldsymbol{\varrho}}{a + \delta q_4} \tag{2.19}$$

Setting the parameters $a = 1$, and $f = 2(a + 1)$ yields a set of Modified

Rodrigues Parameters that are used for this filter. The inverse transformation from $\delta \boldsymbol{p}$ to

$\delta \boldsymbol{q}$ is given by

$$\delta q_4 = \frac{-a\|\delta \boldsymbol{p}\|^2 + f\sqrt{f^2 + (1 - a^2)\|\delta \boldsymbol{p}\|^2}}{f^2 + \|\delta \boldsymbol{p}\|^2} \tag{2.20}$$

$$\delta \boldsymbol{\varrho} = f^{-1}(a + \delta q_4)\delta \boldsymbol{p} \tag{2.21}$$

Position will be represented by latitude, longitude and range from center of the

Moon. Normally height above the surface is used in place of range from center of the

planetary object. However, the Moon is a spheroid and does not have a flattening effect

like the Earth's ellipsoid shape so the range from center of the Moon is used rather than

height above the surface. Velocity will be maintained in a North East Down (NED)

coordinate frame. This type of state is more intuitive and is used frequently with

integrated navigation systems. Biases of the three single axis gyros and accelerometers

complete the rest of the navigation state. All of these parameters make up the state

vector written as

$$\boldsymbol{x} = \begin{bmatrix} \boldsymbol{q}^T & \phi & \lambda & r & v_N & v_E & v_D & \boldsymbol{\beta}_g^T & \boldsymbol{\beta}_a^T \end{bmatrix}^T \tag{2.22}$$

The governing equations of motion for the navigation state are given below.

$$\dot{\hat{\phi}} = \frac{\hat{v}_N}{\hat{R}_m} \tag{2.23}$$

$$\dot{\hat{\lambda}} = \frac{\hat{v}_E}{\hat{R}_m \cos \hat{\phi}} \tag{2.24}$$

$$\dot{\hat{r}} = -\hat{v}_D \tag{2.25}$$

$$\dot{\hat{v}}_N = -\left[\frac{\hat{v}_E}{\hat{R}_m \cos \hat{\phi}} + 2\omega_m\right]\hat{v}_E \sin \hat{\phi} + \frac{\hat{v}_N \hat{v}_D}{\hat{R}_m} + \hat{a}_N \tag{2.26}$$

$$\hat{\dot{v}}_E = \left[\frac{\hat{v}_E}{\hat{R}_m \cos\hat{\phi}} + 2\omega_m\right]\hat{v}_N \sin\hat{\phi} + \frac{\hat{v}_E\hat{v}_D}{\hat{R}_m} + 2\omega_m\hat{v}_D \cos\hat{\phi} + \hat{a}_E \qquad (2.27)$$

$$\hat{\dot{v}}_D = -\frac{\hat{v}_E^2}{\hat{R}_m} - \frac{\hat{v}_N^2}{\hat{R}_m} + 2\omega_m\hat{v}_E \cos\hat{\phi} + g + \hat{a}_D \qquad (2.28)$$

where

$$\hat{\boldsymbol{a}}^N = \begin{bmatrix}\hat{a}_N \\ \hat{a}_E \\ \hat{a}_D\end{bmatrix} = A_B^N(\hat{\boldsymbol{q}})\hat{\boldsymbol{a}}^B \qquad (2.29)$$

$$\hat{\boldsymbol{a}}^B = \tilde{\boldsymbol{a}}^B - \hat{\beta}_a \qquad (2.30)$$

$$\hat{\dot{\beta}}_a = \boldsymbol{0} \qquad (2.31)$$

$$\hat{\dot{\beta}}_g = \boldsymbol{0} \qquad (2.32)$$

The Lidar will provide azimuth, elevation and range in relation from the LRRR. The measurements are converted to Moon Centered-Moon Fixed (MCMF) coordinates before being rotated to NED coordinates. Then the measurements will be processed by the filters and output in latitude, longitude and range from center of the Moon. First the LRRR's latitude and longitude are converted to MCMF using the radius of the Moon.

$$\rho_X^{LRRR} = R_m \cos\phi_{LRRR} \cos\lambda_{LRRR} \qquad (2.33)$$

$$\rho_Y^{LRRR} = R_m \cos\phi_{LRRR} \sin\lambda_{LRRR} \qquad (2.34)$$

$$\rho_Z^{LRRR} = R_m \sin\phi_{LRRR} \qquad (2.35)$$

Next the measurements are converted from azimuth, elevation, and range to NED by the following

$$\rho_N^{obs} = R_m\sin(el) \qquad (2.36)$$

$$\rho_E^{obs} = R_m \cos(el)\sin(az) \qquad (2.37)$$

$$\rho_D^{obs} = R_m \cos(el) \cos(az) \tag{2.38}$$

Then the measurement is rotated to MCMF with

$$\begin{bmatrix} \rho_X^{obs} \\ \rho_Y^{obs} \\ \rho_Z^{obs} \end{bmatrix} = \begin{bmatrix} -\sin\phi_{LRRR}\cos\lambda_{LRRR} & -\sin\lambda_{LRRR} & -\cos\phi_{LRRR}\cos\lambda_{LRRR} \\ -\sin\phi_{LRRR}\sin\lambda_{LRRR} & \cos\lambda_{LRRR} & -\cos\phi_{LRRR}\sin\lambda_{LRRR} \\ \cos\phi_{LRRR} & 0 & \sin\phi_{LRRR} \end{bmatrix} \begin{bmatrix} \rho_N^{obs} \\ \rho_E^{obs} \\ \rho_D^{obs} \end{bmatrix} \tag{2.39}$$

The LRRR vector and measurement vectors are added together to obtain the position of the vehicle in MCMF denoted as S/C.

$$\boldsymbol{\rho}_{MCMF}^{S/C} = \boldsymbol{\rho}_{MCMF}^{obs} + \boldsymbol{\rho}_{MCMF}^{LRRR} \tag{2.40}$$

The above position is input into the filters and subtracted from the estimated position to obtain the residual.

CHAPTER 3

NAVIGATION TECHNIQUES

Extended Kalman Filter

The Extended Kalman Filter is a very common application for nonlinear systems that is used extensively for spacecraft navigation systems. This type of filter assumes the estimated state and the truth state are near to each other. This allows for a first order linearization of the estimate about the mean and covariance to be given as an accurate representation. The probability density function (pdf) of the output estimate can be approximately Gaussian from the linear assumption. Due to the linearization of the system and small error between the estimated and truth state, the EKF has a known problem with filter initialization if there is a large difference between estimated state and the truth.

The EKF utilized for this analysis uses a nonlinear model given in continuous time, which is common for this type of application.

$$\dot{x}(t) = f(x(t), u(t), t) + G(t)w(t), w(t) \sim N(0, Q(t)) \tag{4.1}$$

$$\tilde{y}_k = h(x_k) + v_k, v_k \sim N(0, R_k) \tag{4.2}$$

The algorithm for the EKF begins with initialization of state vector and associated covariance. At each time step, the Kalman gain is calculated. This is defined below along with the sensitivity matrix, $H_k$. The sensitivity matrix transforms measurement state space to navigation state space.

$$H_k(\hat{x}_k^-) = \left.\frac{\partial h}{\partial x}\right|_{\hat{x}_k^-} \tag{4.3}$$

$$K_k = P_k^- H_k^T(\hat{x}_k^-)[H_k(\hat{x}_k^-)P_{2k}^- H_k^T(\hat{x}_k^-) + R_k]^{-1} \tag{4.4}$$

Next the Kalman update of the vehicle state is performed incorporating Lidar measurements. Also the covariance is updated based on the Kalman gain.

$$\hat{x}_k^+ = \hat{x}_k^- + K_k[\tilde{y}_k - h(\hat{x}_k^-)] \tag{4.5}$$

$$P_k^+ = [I - K_k H_k^T(\hat{x}_k^-)]P_k^- \tag{4.6}$$

Then the state and covariance are propagated to the next time step and the process is repeated. The propagation of the state and measurements use a fourth order Runge-Kutta integration scheme. The IMU sensors utilize the model given in equations 2.7 through 2.10 for gyro and accelerometers. The covariance propagation equations can be found in Appendix A.

## Unscented Kalman Filter

Given the extended Kalman filter has a known problem with initialization where the initial state may be far from the truth state, other approaches have been developed. One of these approaches is called the Unscented Kalman Filter developed by Julier, Uhlmann, and Durrant-Whyte [4]. This filter uses the instinct that it is easier to approximate a probability distribution than an arbitrary nonlinear function. The main goal of the UKF is to find a group of points, or sigma points, with a sample probability density function that is similar to the true probability density function. These points are not selected at random but chosen deterministically to yield a mean and covariance. The process captures higher order information than the EKF by using a nonlinear transformation of a select number of points. This type of approach yields an increase accuracy but comes with a computational cost due to the propagation of sigma points.

For the UKF the Kalman filter update equations are rewritten as

$$\hat{x}_k^+ = \hat{x}_k^- + K_k[e_k^-] \tag{4.7}$$

$$P_k^+ = P_k^- - K_k P_k^{e_y e_y} K_k^T \tag{4.8}$$

where $e_k^- \equiv \tilde{y}_k - \hat{y}_k^-$ and the covariance of $e_k^-$ is $P_k^{e_y e_y}$. The Kalman gain is defined as

$$K_k = P_k^{e_x e_y}\left(P_k^{e_y e_y}\right)^{-1} \tag{4.9}$$

The algorithm for the UKF starts with creating a the number of sigma points, $i$, for an augmented state.

$$\sigma_k \leftarrow 2L \text{ columns from } \pm \gamma\sqrt{P_k^a} \tag{4.10}$$

$$\chi_k^{a(0)} = \hat{x}_k^a \tag{4.11}$$

$$\chi_k^{a(i)} = \sigma_k^{(i)} + \hat{x}_k^a \tag{4.12}$$

The augmented state $\hat{x}_k^a$ is defined as

$$x_k^a = \begin{bmatrix} x_k \\ w_k \\ v_k \end{bmatrix}, \quad \hat{x}_k^a = \begin{bmatrix} \hat{x}_k \\ 0_{q\times 1} \\ 0_{m\times 1} \end{bmatrix} \tag{4.13}$$

where $L$ is the size of the vector $\hat{x}_k^a$. The parameter $\gamma$ is

$$\gamma = \sqrt{L + \lambda} \tag{4.14}$$

and the composite scaling parameter $\lambda$ is

$$\lambda = \alpha^2(L + \kappa) - L \tag{4.15}$$

where $\alpha$ determines the spread of the sigma points and $\kappa$ is used to take advantage of knowledge about higher moments of a distribution. The square root of the above covariance matrix is determined by using the Cholesky decomposition.

The weights used for the calculating estimates of the mean and covariance are given as

$$W_0^{mean} = \frac{\lambda}{L + \lambda} \tag{4.16}$$

$$W_0^{cov} = \frac{\lambda}{L + \lambda} + (1 - \alpha^2 + \beta) \tag{4.17}$$

16

$$W_i^{mean} = W_i^{cov} = \frac{1}{2(L + \lambda)}, \qquad i = 1,2,\dots,2L \tag{4.18}$$

where $\beta$ is a parameter used to incorporate prior knowledge of the distribution. The augmented state with sigma points are propagated to the next measurement time step. The estimation for the current measurement is calculated. Then the calculation of the prediction for state, covariance and measurement are determined from the weighting of the sigma points.

$$\widehat{\boldsymbol{x}}_k^- = \sum_{i=0}^{2L} W_i^{mean} \boldsymbol{\chi}_k^{x(i)} \tag{4.19}$$

$$\boldsymbol{P}_k^- = \sum_{i=0}^{2L} W_i^{cov} \big[ \boldsymbol{\chi}_k^{x(i)} - \widehat{\boldsymbol{x}}_k^- \big]\big[ \boldsymbol{\chi}_k^{x(i)} - \widehat{\boldsymbol{x}}_k^- \big]^T \tag{4.20}$$

$$\widehat{\boldsymbol{y}}_k^- = \sum_{i=0}^{2L} W_i^{mean} \gamma_k^{(i)} \tag{4.21}$$

$$\gamma_k^{(i)} = \boldsymbol{h}\big(\boldsymbol{\chi}_k^{x(i)}, \boldsymbol{u}_k, \boldsymbol{\chi}_k^{v(i)}, k\big) \tag{4.22}$$

The filter gain in equation 4.9 is determined through the following covariance and cross correlation matrix equations.

$$\boldsymbol{P}_k^{yy} = \sum_{i=0}^{2L} W_i^{cov} \big[ \gamma_k^{(i)} - \widehat{\boldsymbol{y}}_k^- \big]\big[ \gamma_k^{(i)} - \widehat{\boldsymbol{y}}_k^- \big]^T \tag{4.23}$$

$$\boldsymbol{P}_k^{e_y e_y} = \boldsymbol{P}_k^{yy} + \boldsymbol{R}_k \tag{4.24}$$

$$\boldsymbol{P}_k^{e_x e_y} = \sum_{i=0}^{2L} W_i^{cov} \big[ \boldsymbol{\chi}_k^{x(i)} - \widehat{\boldsymbol{x}}_k^- \big]\big[ \gamma_k^{(i)} - \widehat{\boldsymbol{y}}_k^- \big]^T \tag{4.25}$$

The filter updates the state vector using equation 4.7 with the gain determined above. Then the process is repeated for each measurement time step.

CHAPTER 4

SIMULATION

Trajectory

The initial state given in Keplerian elements in Table 4-1 is a post-Translunar

Injection (TLI) burn vector.  The orbit will place the vehicle on a free return trajectory from

the Moon.  This is based on data from the Apollo 11 mission.

Table 4-1 Keplerian Elements for Initial State

| Parameter Description | Value |
| --- | --- |
| Semi-major Axis, km | 286535.8 |
| Eccentricity | 0.976965 |
| Inclination, deg | 31.383 |
| Argument of Periapse, deg | 4.4102 |
| Longitude of Ascending Node, deg | 358.380 |
| Time of Periapse, sec | 10054 |

For the cislunar trajectory propagation of the truth state, perturbations to the orbit

included a gravity model and third body accelerations [6].  The truth used the degree and

order of 32x32 harmonic coefficient EGM96 model.  The filters used in this analysis

propagated with 4x4 EGM96 (Earth Gravity Model) coefficients.  The lunar orbit trajectory

for the truth state used the 32x32 harmonic coefficients from the GRAIL 660 (ref) lunar

gravity model (Gravity Recovery And Interior Laboratory) while the filter propagated with

the 4x4 coefficients.  Using a less accurate model for gravity for spacecraft is typical in

order to keep an accurate enough estimate to satisfy trajectory requirements while

keeping computational cost down.

A patched conic approximation was used to determine time of flight until the

vehicle entered the Moon's gravity sphere of influence.  During this time measurements

were generated at approximately six hours post-TLI and also around the 12 hour mark.

Star selection was based on those used during Apollo missions and are listed in Table 4-

2.  The vehicle was propagated until it entered the Moon's gravitational sphere of influence known to be 66,100 km from the Moon.  Then the spacecraft was placed on a hyperbolic trajectory to the Moon.  Once at the time of closest approach to the Moon, the vehicle was assumed to perform a burn to place it into a 315x200 km orbit.  After two orbit the orbit was circularized to 200x200 km.  These heights were selected to provide views of the LRRRs for tracking purposes during each orbit of the Moon.  Lidar measurements were generated for the lunar orbits using the LRRRs on the lunar surface. The LRRR locations are listed in Table 4-3.  Tracking arcs were generated based on line of sight of the spacecraft to the LRRR through determination of line of sight Acquisition of Satellite (AOS) and Loss of Satellite (LOS) times for each LRRR.   Tracking arcs were generally around 16 minutes in length.  It was determined that the Apollo 11 and 15 LRRRs provided similar tracking arcs.  The Apollo 14 LRRR provides additional line of sight coverage.  Therefore, the spacecraft could point at the Apollo 11 LRRR then rotate and point at the Apollo 14 LRRR.  This allows for a larger section of the orbit to be measured.

Table 4-2 Star and Earth Locations

| Star | Celestial Latitude (deg N) | Celestial Longitude (deg E) |
|---|---|---|
| Altair | 30 | 302 |
| Diphda | -22 | 2 |
| Earth | -4 | 326 |

Table 4-3 Lunar Ranging Retroreflector Locations

| Mission | Lunar Latitude (deg N) | Lunar Longitude (deg E) |
|---|---|---|
| Apollo 11 | 0.67377 | 23.47293 |
| Apollo 14 | -3.64422 | -17.47880 |
| Apollo 15 | 26.13333 | 3.62837 |

A pitch rate 0.05 degree per second was applied through the tracking arc to emulate the vehicle tracking the LRRR on the lunar surface.

Filters

The filters were coded in MATLAB. They employed an ode45 solver for propagation. The propagation step was set to 10 seconds since the measurements were taken at the same interval for both cislunar and lunar orbit. For the cislunar portion, the tracking arc was over a 10 minute period at the 10 second interval. These periods occurred around six and twelve hours after the TLI burn, which is consistent with the times of midcourse burns during Apollo transit to the Moon. For the lunar portion, the tracking arcs were based on line of sight. This time interval is consistent with ground-based radar output from the DSN.

For the cislunar trajectory, star tracker angle measurements were generated at 10 second intervals during the two ten minute selection periods identified earlier with an accuracy of 0.01 deg. The initial covariance was set fairly large in position due to the distance of the vehicle from the Earth at 130 km in position with a velocity of 10 m/s.

During lunar orbit, tracking measurements were synthesized every 10 seconds. This meant the gyro and accelerometer sensors were sampled at the same rate. The gyro and accelerometer noise parameters detailed in Chapter 3 were set to $\boldsymbol{\eta}_{gv} = \sqrt{10} \times 10^{-7}$ rad/sec$^{1/2}$, $\boldsymbol{\eta}_{gu} = \sqrt{10} \times 10^{-10}$ rad/sec$^{3/2}$, $\boldsymbol{\eta}_{av} = 1.62 \times 10^{-7}$ m/sec$^{3/2}$, and $\boldsymbol{\eta}_{au} = 6 \times 10^{-5}$ m/sec$^{5/2}$. The initial biases for the gyro and accelerometer were 0.01 deg/hr and 0.003 m/sec$^2$, respectively. The Lidar sensor data provided an accuracy of .01 deg in angle and 10 meter in range. The initial covariance values were set to 0.33 deg/axis for attitude, 0.1 radians for latitude and longitude, 5 km for range, 0.1 km/s for velocity, 1 deg/hr for gyro bias, and 0.005 m/s$^2$ for accelerometer bias.

The UKF parameters were set to appropriate values for this analysis (equations 4.15 and 4.17). For cislunar estimation, alpha ($\alpha$) was set to one for maximum spread of the sigma points. Beta ($\beta$) was set to two and kappa ($\kappa$) was set to zero. The lunar orbit estimation used the same values for beta and kappa, however, the alpha parameter was reduced to 0.1. This improved the attitude estimation of the given system. A smaller alpha value that reduces the spread of the sigma points is considered acceptable given an assumed Gaussian distribution.

CHAPTER 5

SIMULATION RESULTS

Cislunar Trajectory

The MC1 and MC2 cases were able to show that a vehicle can provide a good estimation of the vehicle state using celestial navigation techniques in the form of planet-star angles and planet angular diameter. Figures 5-1 through 4 plot the errors in Earth Centered Inertial (ECI) coordinates for both EKF and UKF and provide similar results for the MC1 case. They compare the estimated state to the truth and associated covariance error. The large covariance error associated with the position estimate is expected since a small error in angle measurement can result in large range error at the range the vehicle is from the Earth. Comparison of the output of both filter estimate versus the truth is shown in Figures 5-5 and 5-6 show the EKF and UKF have similar estimates.
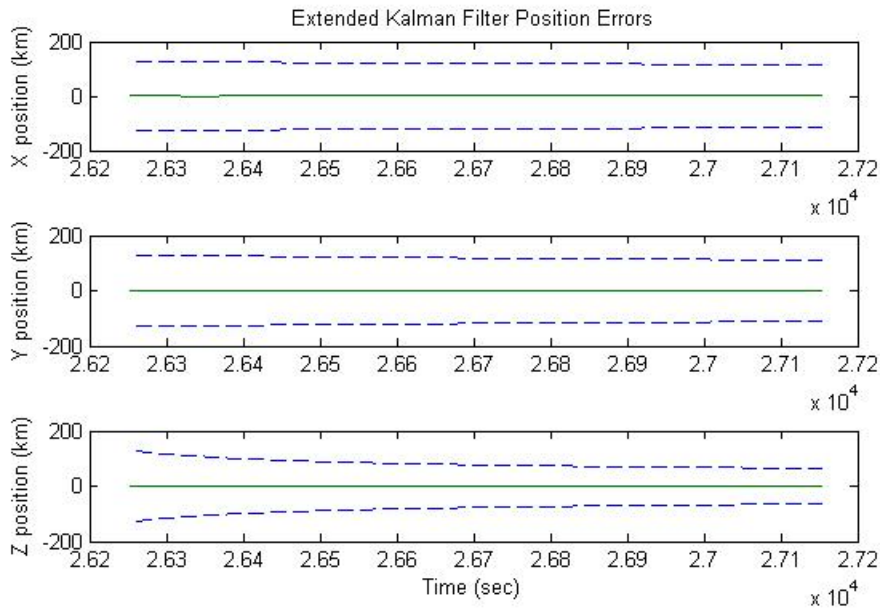


Figure 5-1 MC1 EKF Position Errors (TLI+6 hrs)

22
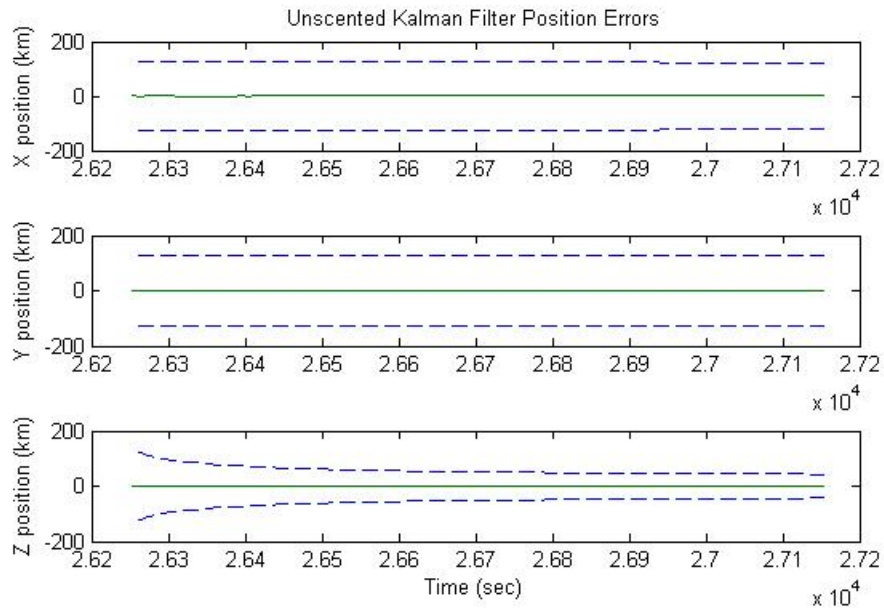
Figure 5-2 MC1 UKF Position Errors (TLI+6 hrs)
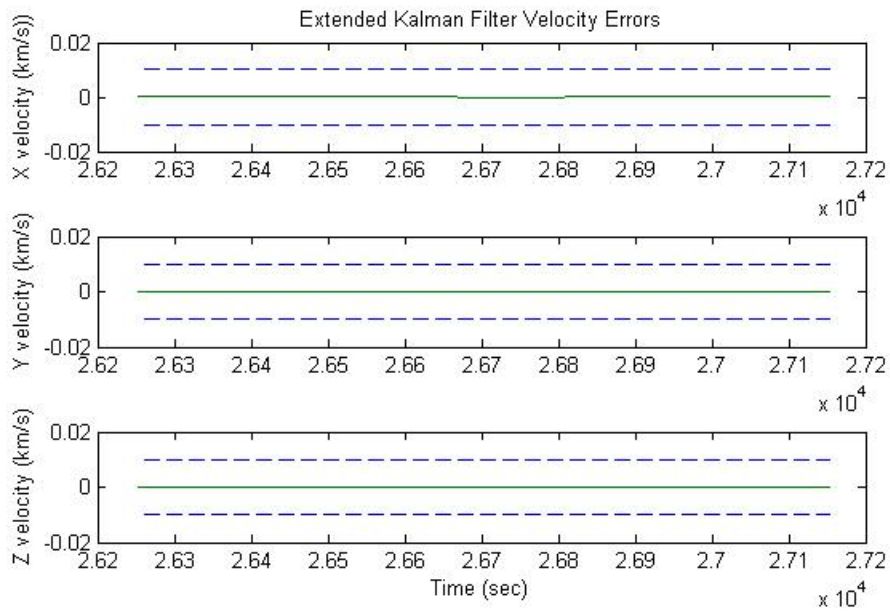


Figure 5-3 MC1 EKF Velocity Errors (TLI+6 hrs)

23
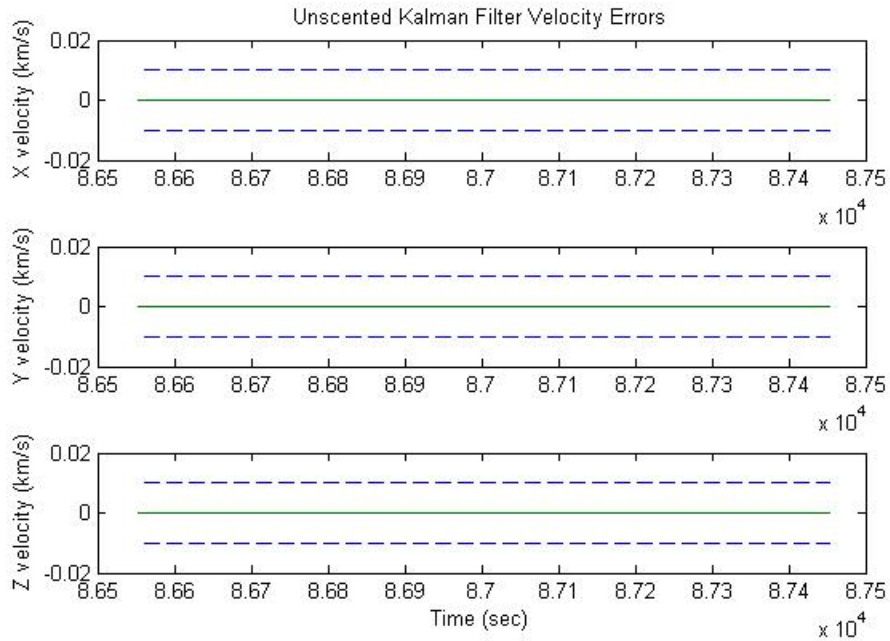
Figure 5-4 MC1 UKF Velocity Errors (TLI+6 hrs)
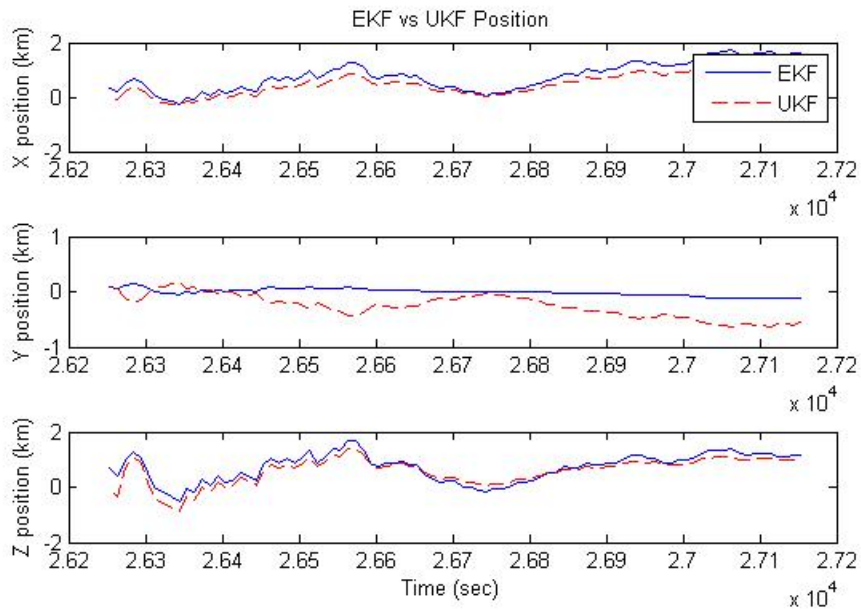


Figure 5-5 MC1 Filter Position Estimation Compare (TLI+6 hrs)
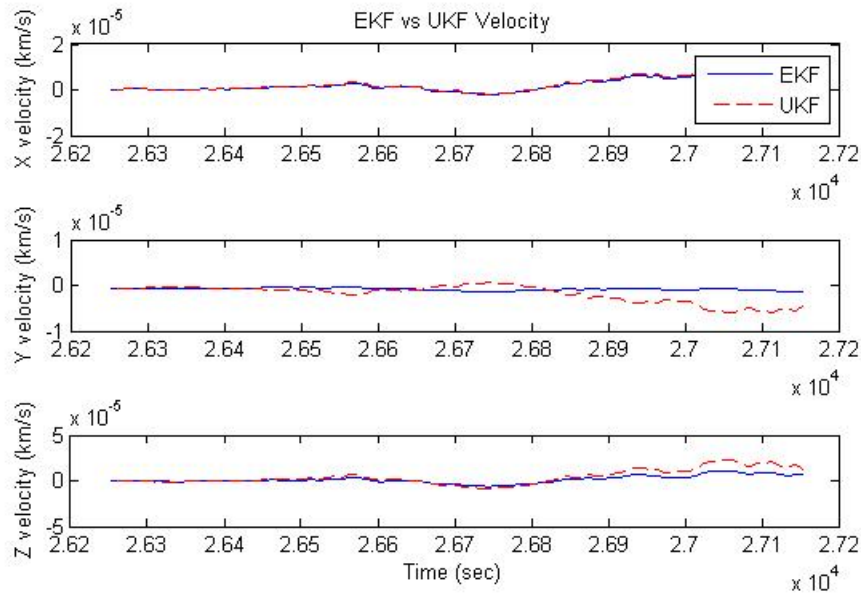
Figure 5-6 MC1 Velocity Estimation Compare (TLI+6 hrs)

The MC2 case was about twelve hours after TLI and provided similar estimation and associated error to the MC1 timeframe for both filters.  Figures 5-7 through 10 show filter error.  Figures 5-11 and 5-12 compare the estimation the filters position and velocity.  Both filters show that the error in the estimate is larger than MC1 case.  Since the vehicle is much further away from the Earth, this amount of error is expected.  As the vehicle travels farther away from the Earth, noise in the measurement will show an increase in estimated error.  This can be offset by taking measurement using the Moon since the spacecraft will be approaching this planetary body.
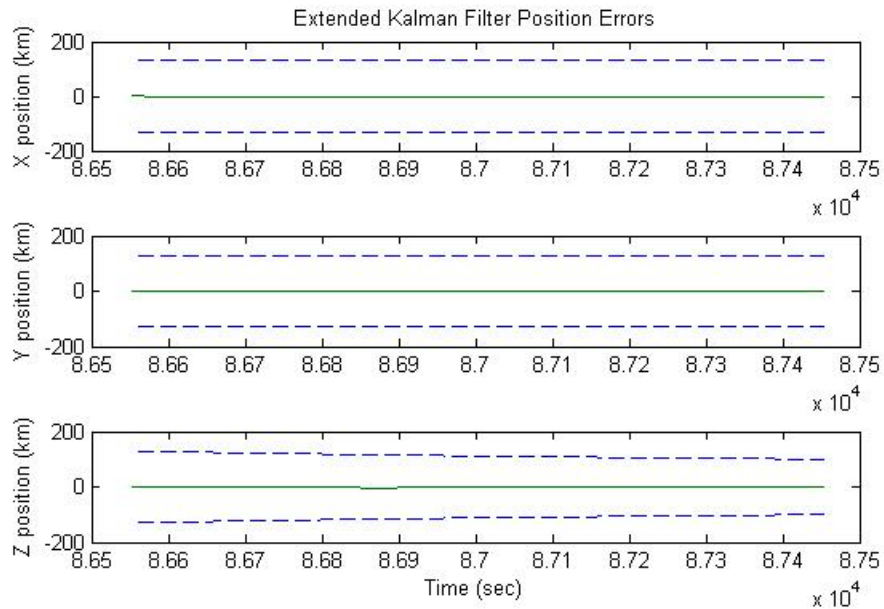
Figure 5-7 MC2 EKF Position Errors (TLI+12 hrs)
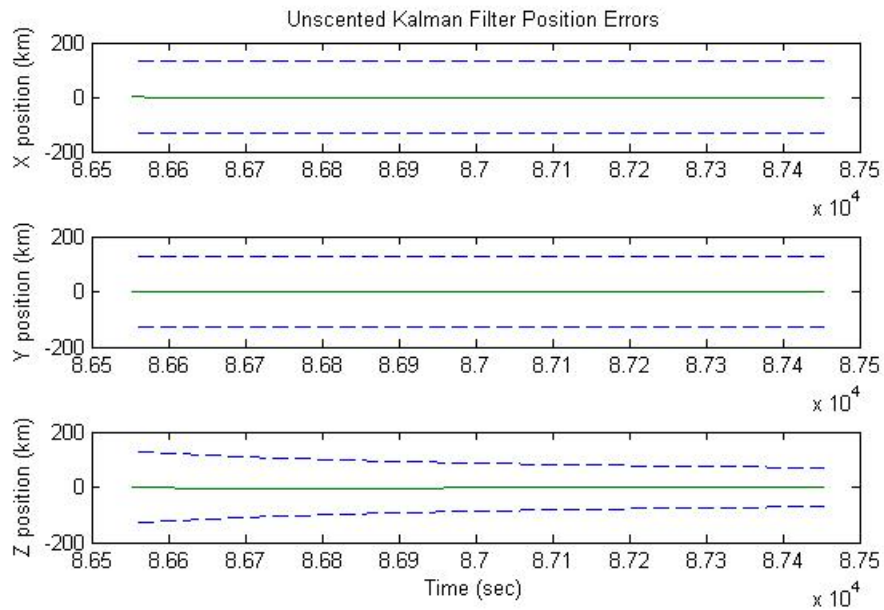


Figure 5-8 MC2 UKF Position Errors (TLI+12 hrs)
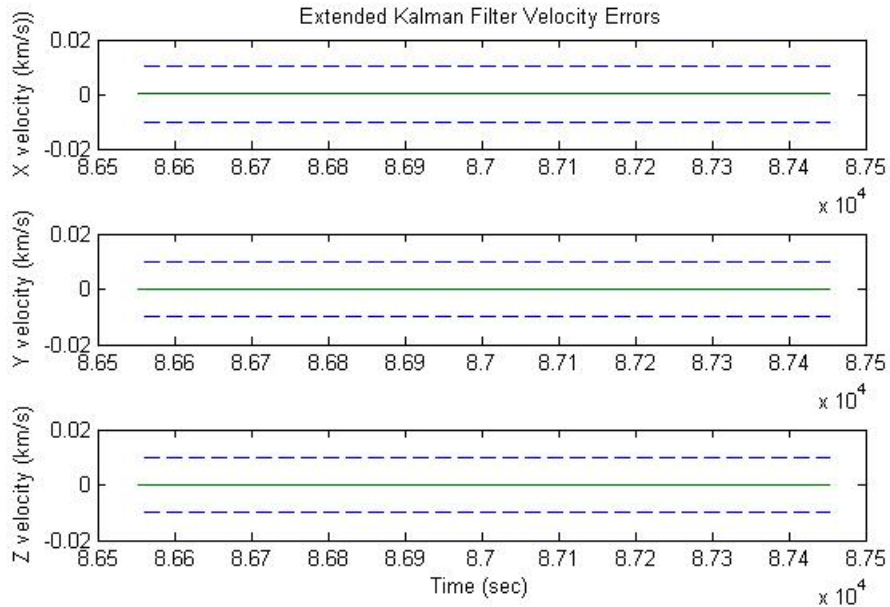
Figure 5-9 MC2 EKF Velocity Errors (TLI+12 hrs)
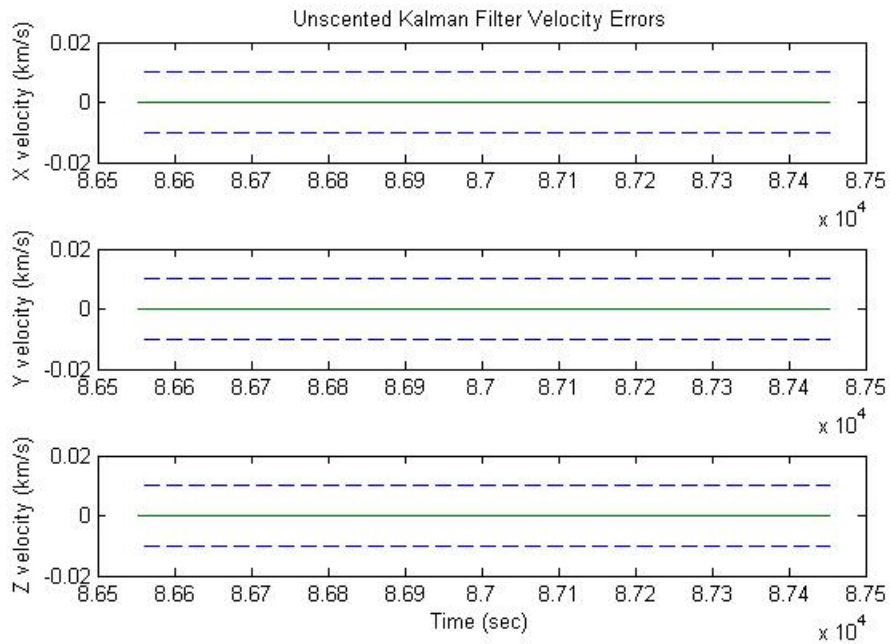


Figure 5-10 MC2 UKF Velocity Errors (TLI+12 hrs)

27
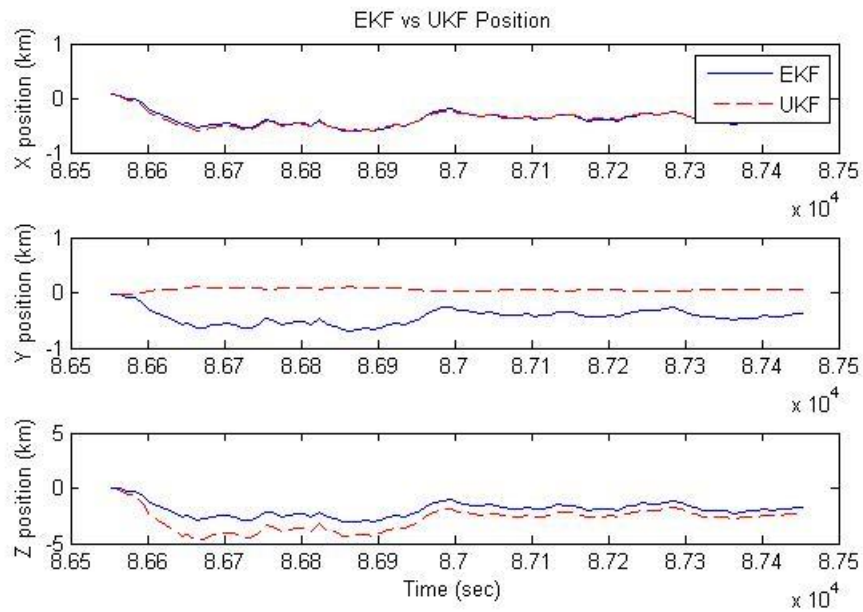
Figure 5-11 MC2 Position Estimation Compare (TLI+12 hrs)
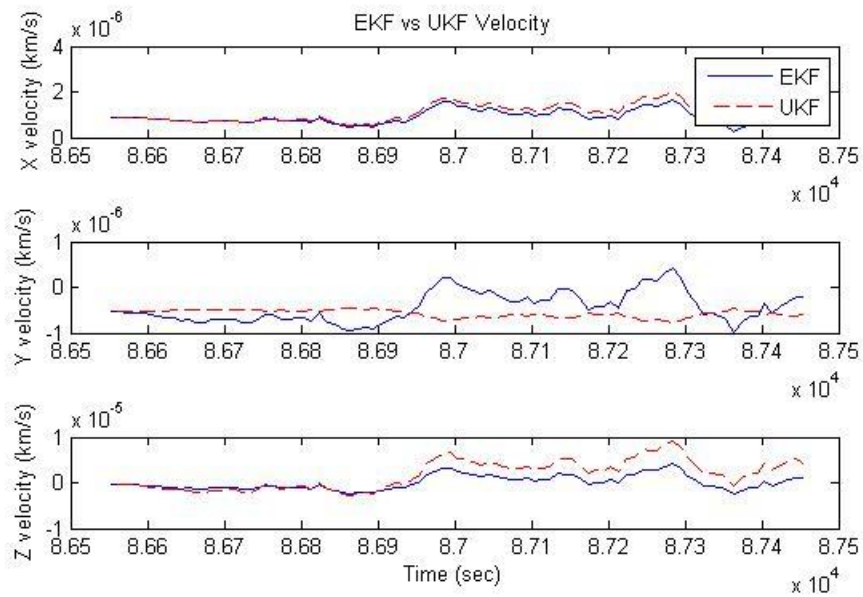


Figure 5-12 MC2 Velocity Estimation Compare (TLI+12 hrs)

The EKF and UKF performed well for both MC1 and MC2 cases.  The UKF performed slightly better than the EKF in the Z-axis with respect to 1-sigma performance. Also, the UKF appeared to be sensing better in the Y-axis.  The Y-position did not vary much and the EKF shows little affect to input as opposed to the other axes.

Lunar Orbit

The autonomous vehicle utilized an integrated navigation system once lunar orbit was achieved.  Estimate of the attitude was needed to ensure the vehicle's Lidar is pointed accurately at the LRRRs on the lunar surface.  Gyro and accelerometer data were incorporated along with the Lidar ranging measurements to provide attitude, position and velocity.  Gyro and accelerometer biases were estimated as well.  The filters were analyzed for an elliptical orbit (315x200 km) and circular orbit (200x200 km). Tracking passes for each orbit were examined for a total of four measurement (2 per type of orbit) gathering periods along with both EKF and UKF processing the data.  The first tracking pass tracking was initialized with the truth state.  The state estimate at the end of the first tracking pass was propagated to the next tracking pass on the following orbit. This used a 4x4 gravitational model.  This was performed to ensure the filters would perform well under ideal conditions for the first pass and realistic conditions for the second pass.

For discussion purposes here the first tracking pass of the elliptical orbit will be examined.  The output for all tracking arcs were similar even with the slight offset in initial state for the second tracking pass of each orbit.  The data for the three other periods are included in Appendices C, D and E.

The filter output estimates showed good performance in attitude. The filters were within 0.1 deg of each other. Figures 5-13 and 5-14 show error bounded by the 3-sigma performance. Figure 5-15 compares the attitude output of the filters.
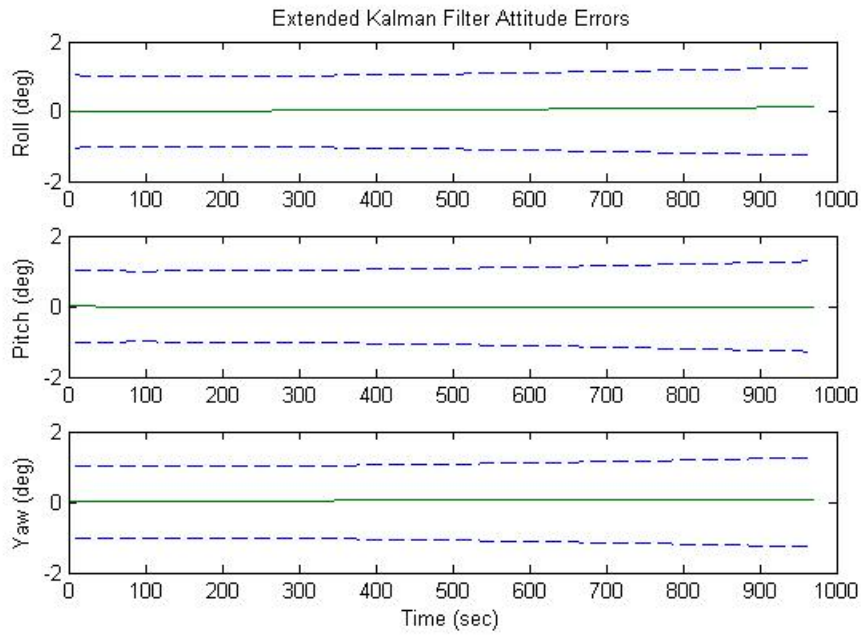


Figure 5-13 Elliptical Orbit 1 EKF Attitude Error
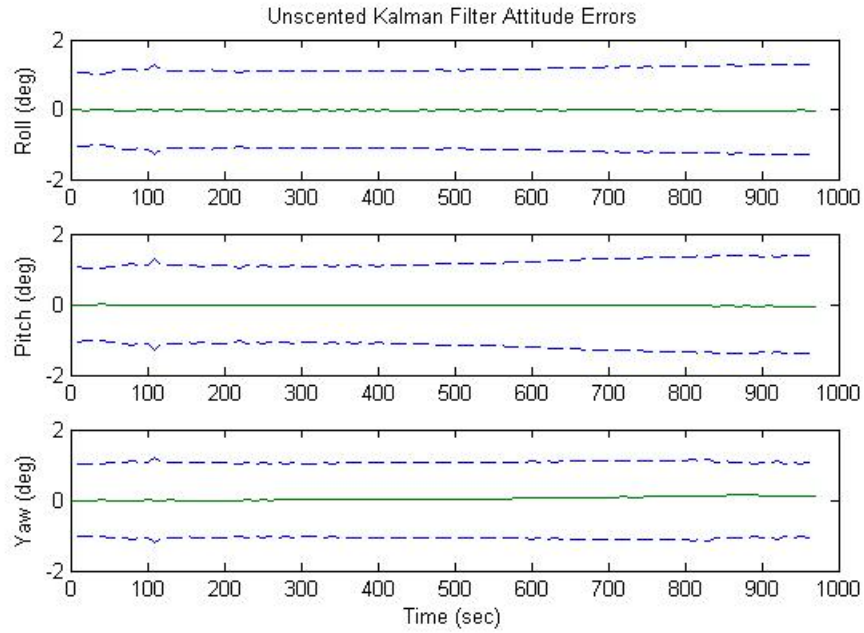
Figure 5-14 Elliptical Orbit 1 UKF Attitude Error
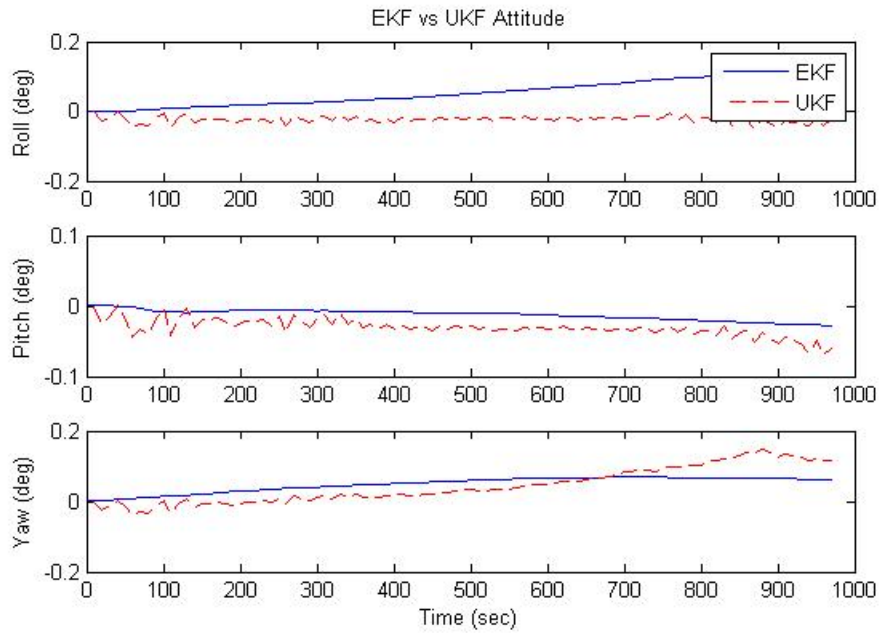


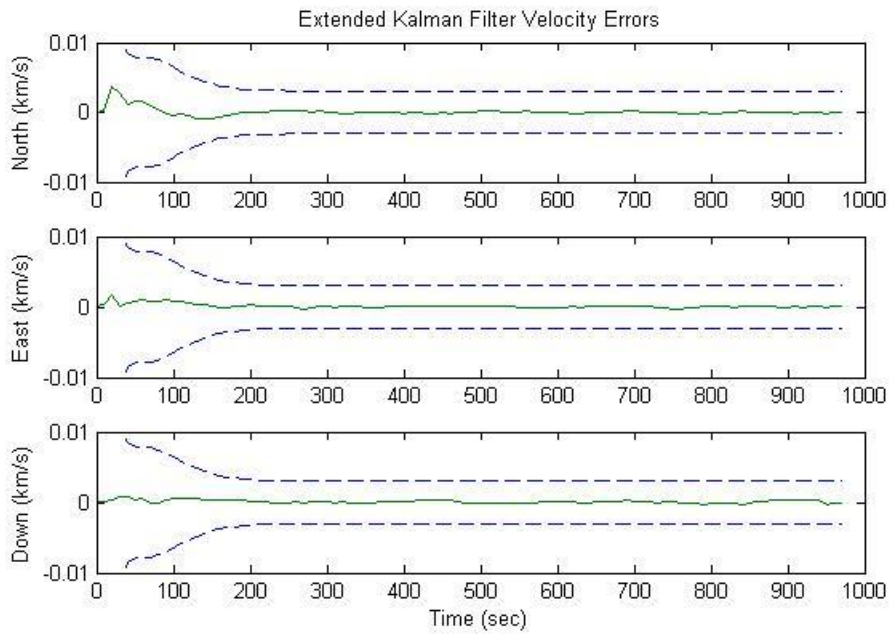Figure 5-15 Elliptical Orbit 1 EKF vs UKF Attitude Error

The position estimates for both filter performed very well. Figures 5-16 and 5-17 illustrate this. The latitude and longitude output shown in Figure 5-18 show $10^{-3}$ error in latitude and longitude and under 50-meter accuracy in range.
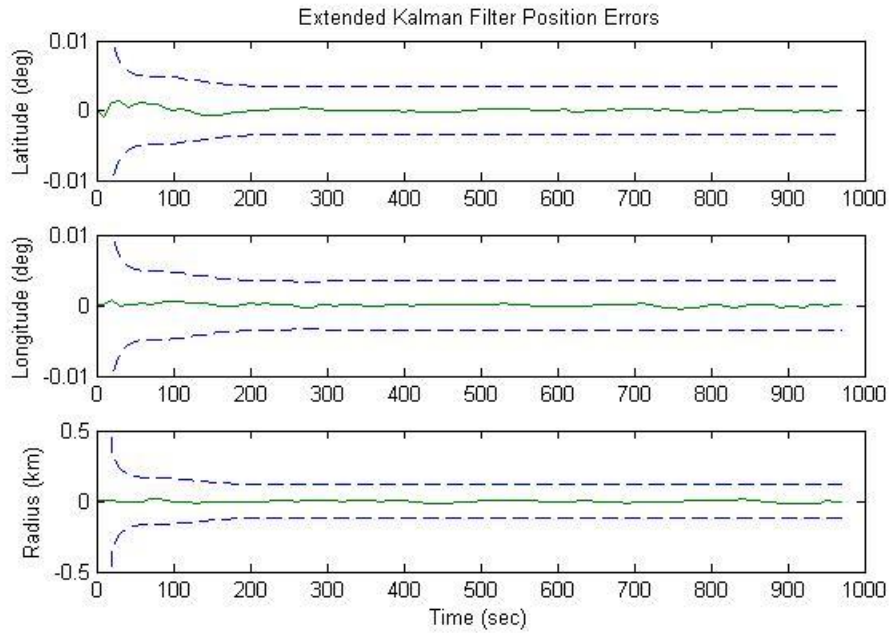


Figure 5-16 Elliptical Orbit 1 EKF Position Error
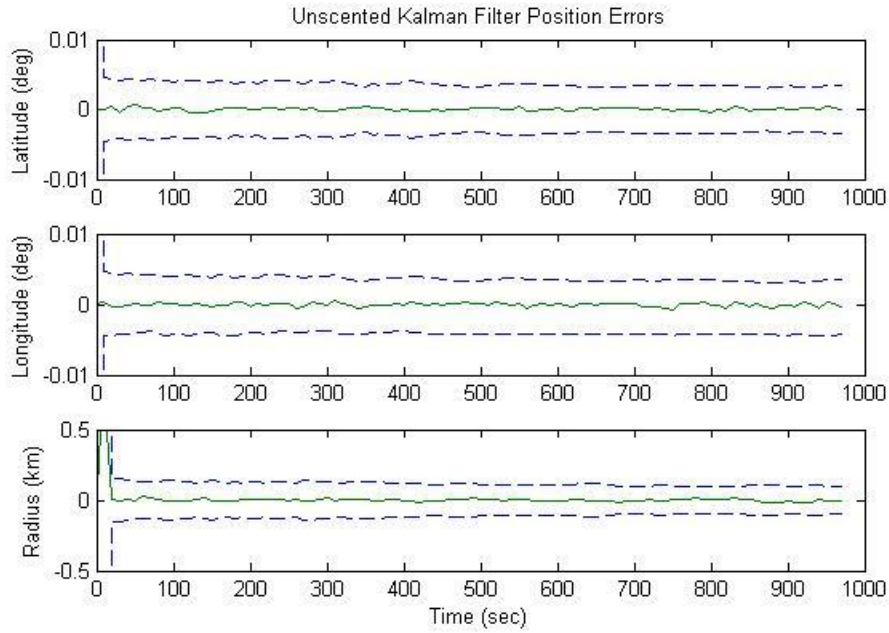
Figure 5-17 Elliptical Orbit 1 UKF Position Error
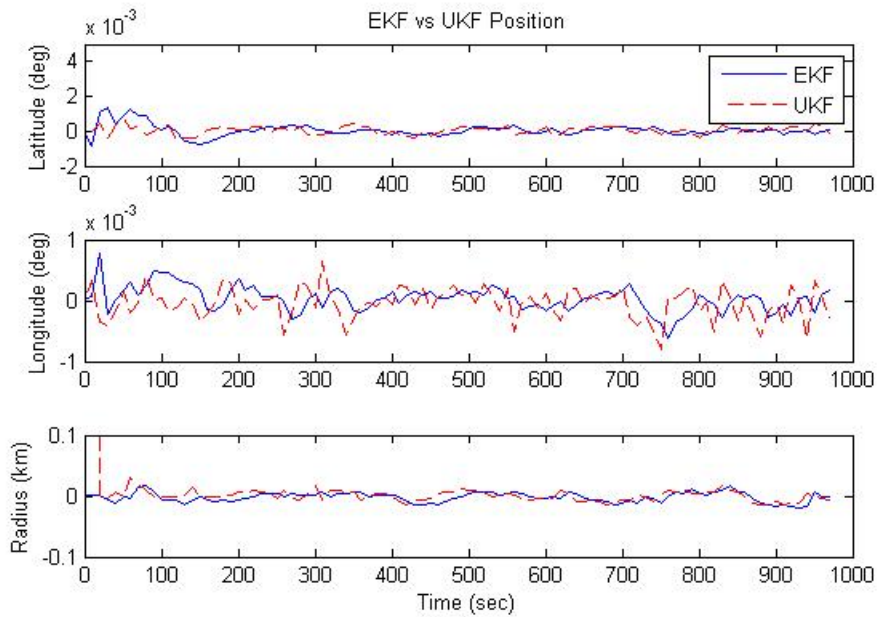


Figure 5-18 Elliptical Orbit 1 EKF vs UKF Position Error

The velocity components of the state performed well.  The UKF velocity was sensitive to position measurement noise.  Velocity determined from position measurements can cause inconsistencies with its determination.  The UKF converged quickly, but as the tracking pass proceeded the 3-sigma performance varied as position measurements were processed.  Also, the system modeled velocity in local NED coordinates for this analysis. Modeling in a Moon Center Moon Fixed coordinate system could provide better results.



Figure 5-19 Elliptical Orbit 1 EKF Velocity Error
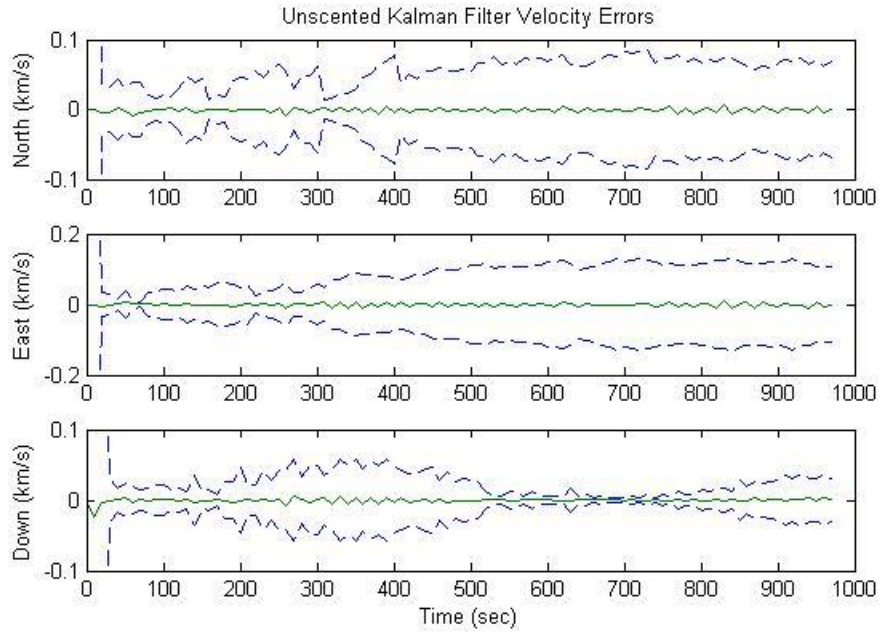
Figure 5-20 Elliptical Orbit 1 UKF Velocity Error
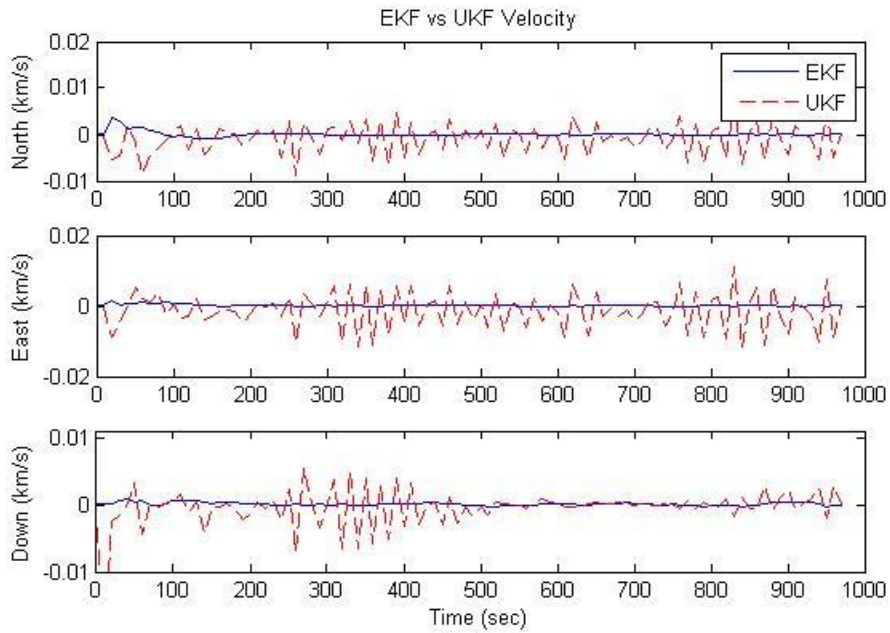


Figure 5-21 Elliptical Orbit 1 EKF vs UKF Velocity Error

The gyro and accelerometer biases are given in Figures 5-22 through 25. The filters were able to track the small amount of initial bias input into the system. The gyro bias 3-sigma performance was large and could perform better with filter tuning to the system.
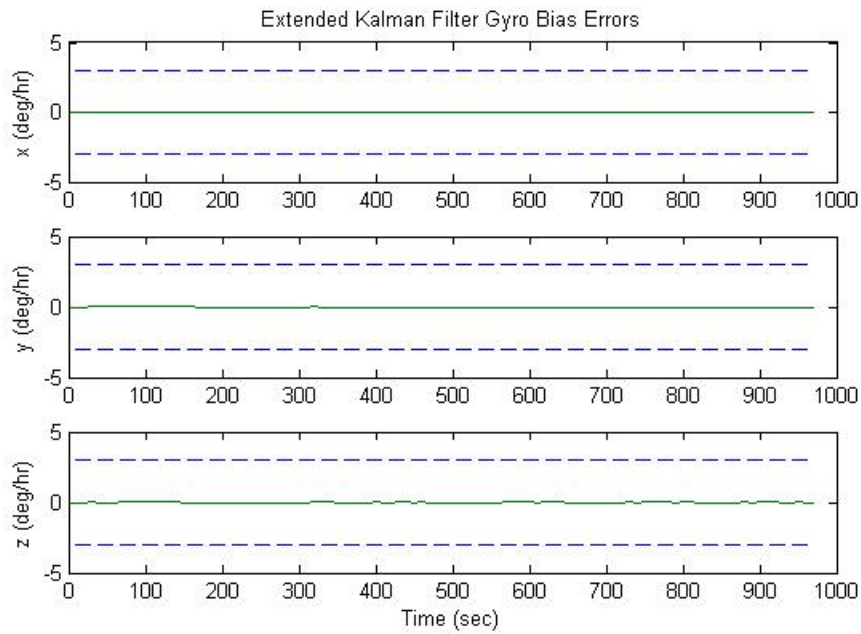


Figure 5-22 Elliptical Orbit 1 EKF Gyro Bias
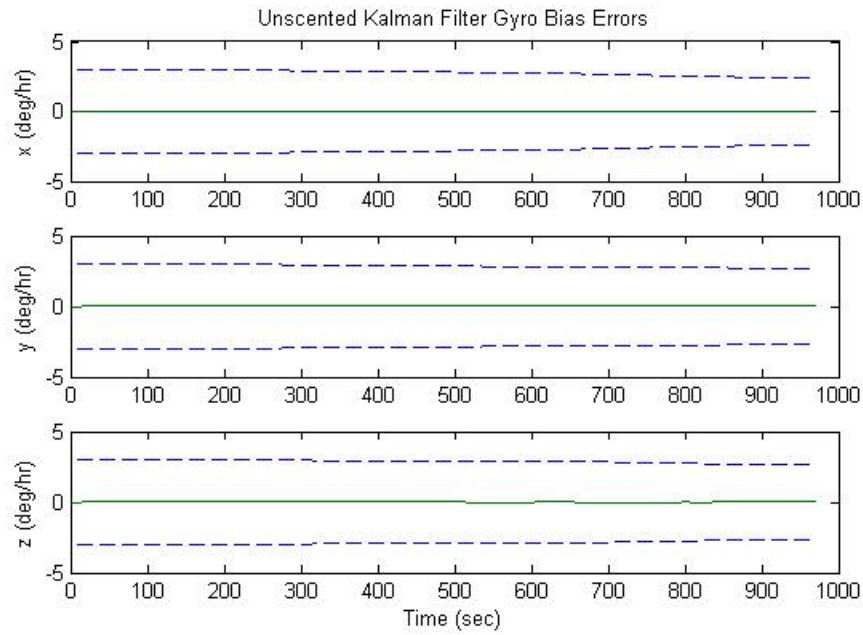
Figure 5-23 Elliptical Orbit 1 UKF Gyro Bias
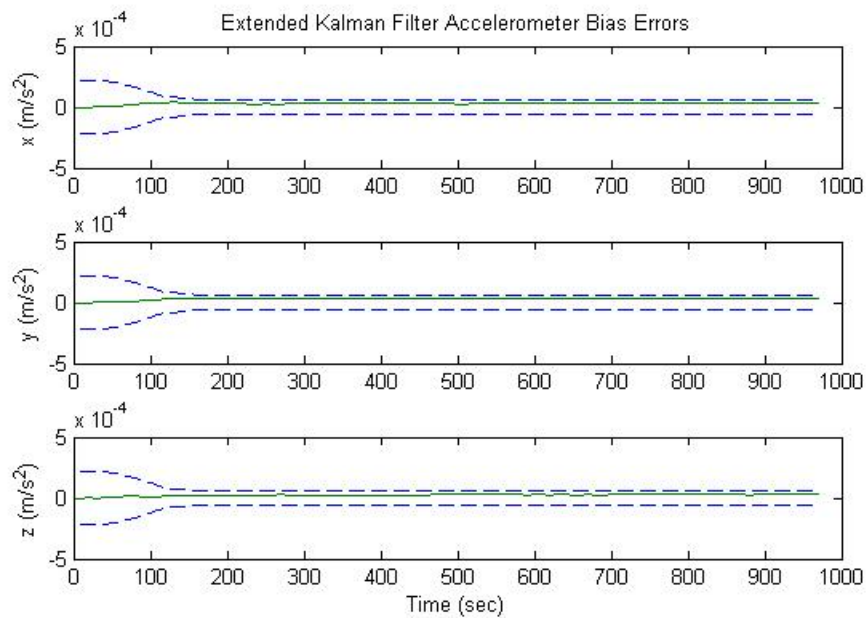


Figure 5-24 Elliptical Orbit 1 EKF Accelerometer Bias
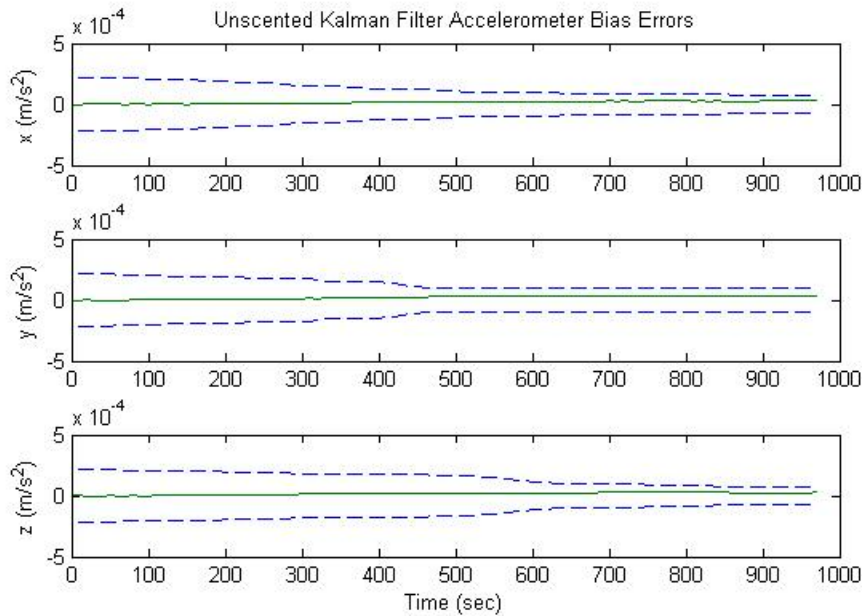
Figure 5-25 Elliptical Orbit 1 UKF Accelerometer Bias

Overall the EKF and UKF performed similarly. The UKF was not as well behaved in velocity than the EKF. The UKF is expected to perform as well or better than the EKF. However, the UKF is more sensitive to measurements than the EKF and can benefit from more analysis to tune the UKF filter to the system. This scope of this analysis was to perform an initial assessment of the filters and determine the feasibility of each one. As such, both filters perform well for the given task with the EKF providing a slightly better state estimate for propagation to the next tracking arc.


Computational Speed

The last piece of this analysis was to examine the computational speed for the cislunar filters and the lunar orbit filters. This helps assess which filter to implement for real-time operations. The filter used an ode45 solver in Matlab for the propagator. This increased the computation burden on the UKF tremendously as expected. The UKF

38

propagates its n-element state 2n+1 times compared to the single propagation of the EKF. This leads to large time differences for the lunar orbit filter. Table 5-1 shows the average time the filter took to process each measurement in seconds.

Table 5-1 Filter Computational Speed

| Tracking Case | EKF | UKF |
|---|---|---|
| MC1 | 0.9006 | 9.9389 |
| MC2 | 0.7509 | 10.2349 |
| Elliptical Orbit 1 | 1.1691 | 35.3384 |
| Elliptical Orbit 2 | 1.0413 | 32.6466 |
| Circular Orbit 1 | 1.1208 | 32.0274 |
| Circular Orbit 2 | 1.0636 | 32.5209 |

The 10 second sampling rate for all tracking periods during cislunar transit and lunar orbit was 10 seconds. Therefore, the EKF would be selected for processing real-time. A different propagator can be used such as an RK4 (fourth order Runge-Kutta) to reduce computational time for the UKF. Also, parallel processing could be investigated as a reduction measure.

CHAPTER 6

CONCLUSION AND FUTURE WORK

This thesis presents an initial investigation into using available navigation techniques as a way to place autonomous vehicle in orbit about the Moon. The use of laser ranging from the lunar surface located LRRRs provide an acceptable means of maintaining a navigation state in lunar orbit without relying on the DSN to provide tracking data. This approach should be considered for future projects involving lunar orbit operations. This should keep operational costs low for a lunar orbit mission.

Applying either Kalman filter to celestial navigation provides method suitable for spacecraft navigation during cislunar transit to the Moon. Both filters processing of Lidar measurements yield excellent results. The EKF is more suitable due to computational performance for the given measurement time interval.

Future work of this analysis can be performed through tuning of the system to particular sensors. Lidar sensor evaluation for LRRR application can be investigated. Evaluation of equations of motion in a Moon-centered rotational coordinate system could provide better results than the one in this analysis. Using other means of propagation or parallel processing architecture could be investigated to increase computational speed of the UKF.

Another promising filter application that was not addressed in this analysis is the Rao-Blackwellized Particle Filter (RBPF). The RBPF seeks to provide a more accurate estimation due to the large sampling of data points processed at each time step to give a better approximation. Partitioning the state into nonlinear and linear part using the Rao-Blackwell theorem. The number of sampling points is reduced versus a conventional

40

particle filter thus lowering the computational load associated with propagating each

particle.  The formulation for the RPBF is included in Appendix F.

APPENDIX A:

EXTENDED KALMAN FILTER COVARIANCE PROPAGATION

The covariance propagation for the EKF is given by the equation

$$\Delta \dot{x} = F\Delta x + Gw \tag{A.1}$$

The state, error state vector and process noise for the navigation system used during cislunar transit are defined by

$$\Delta x = \begin{bmatrix} p \\ v \end{bmatrix}, \qquad \Delta x = \begin{bmatrix} \Delta p \\ \Delta v \end{bmatrix}, \qquad w = \begin{bmatrix} \eta_p \\ \eta_v \end{bmatrix} \tag{A.2}$$

The state transition matrix and process noise transform are

$$F = \begin{bmatrix} 0_{3\times3} & I_{3\times3} \\ F_{21} & 0_{3\times3} \end{bmatrix} \tag{A.3}$$

$$G = \begin{bmatrix} I_{3\times3} & 0_{3\times3} \\ 0_{3\times3} & I_{3\times3} \end{bmatrix} \tag{A.4}$$

with $F_{21}$ defined as

$$F_{21} = \begin{bmatrix} \dfrac{3\mu x^2}{\|r\|^5} - \dfrac{\mu}{\|r\|^3} & \dfrac{3\mu xy}{\|r\|^5} & \dfrac{3\mu xz}{\|r\|^5} \\ \dfrac{3\mu xy}{\|r\|^5} & \dfrac{3\mu y^2}{\|r\|^5} - \dfrac{\mu}{\|r\|^3} & \dfrac{3\mu yz}{\|r\|^5} \\ \dfrac{3\mu xz}{\|r\|^5} & \dfrac{3\mu yz}{\|r\|^5} & \dfrac{3\mu z^2}{\|r\|^5} - \dfrac{\mu}{\|r\|^3} \end{bmatrix} \tag{A.5}$$

The state, error state vector and process noise for the integrated navigation system used during lunar orbit are defined by

$$\Delta x = \begin{bmatrix} q \\ p \\ v^N \\ \beta_g \\ \beta_a \end{bmatrix}, \qquad \Delta x = \begin{bmatrix} \delta\alpha \\ \Delta p \\ \Delta v^N \\ \Delta\beta_g \\ \Delta\beta_a \end{bmatrix}, \qquad w = \begin{bmatrix} \eta_{gv} \\ \eta_{gu} \\ \eta_{av} \\ \eta_{au} \end{bmatrix} \tag{A.6}$$

The state transition matrix and process noise transform are

$$F = \begin{bmatrix} F_{11} & F_{12} & F_{13} & -I_{3\times3} & 0_{3\times3} & F_{16} & 0_{3\times3} \\ 0_{3\times3} & F_{22} & F_{23} & 0_{3\times3} & 0_{3\times3} & 0_{3\times3} & 0_{3\times3} \\ F_{31} & F_{32} & F_{33} & 0_{3\times3} & F_{35} & 0_{3\times3} & F_{37} \\ 0_{3\times3} & 0_{3\times3} & 0_{3\times3} & 0_{3\times3} & 0_{3\times3} & 0_{3\times3} & 0_{3\times3} \\ 0_{3\times3} & 0_{3\times3} & 0_{3\times3} & 0_{3\times3} & 0_{3\times3} & 0_{3\times3} & 0_{3\times3} \end{bmatrix} \tag{A.7}$$

$$G = \begin{bmatrix} -I_{3\times3} & 0_{3\times3} & 0_{3\times3} & 0_{3\times3} \\ 0_{3\times3} & 0_{3\times3} & 0_{3\times3} & 0_{3\times3} \\ 0_{3\times3} & 0_{3\times3} & -A_B^N(\hat{q})I_{3\times3} & 0_{3\times3} \\ 0_{3\times3} & 0_{3\times3} & 0_{3\times3} & 0_{3\times3} \\ 0_{3\times3} & 0_{3\times3} & 0_{3\times3} & 0_{3\times3} \end{bmatrix} \tag{A.8}$$

The parts of the state transition matrix, F, identified above are defined as

$$F_{11} = -\left[\left(\tilde{\boldsymbol{\omega}}_{B/I}^B - \hat{\boldsymbol{\beta}}_g\right) \times\right] \tag{A.9}$$

$$F_{12} = -A_N^B(\hat{q}) \left.\frac{\partial \boldsymbol{\omega}_{N/I}^N}{\partial \boldsymbol{p}}\right|_{\hat{\boldsymbol{p}}, \hat{\boldsymbol{v}}^N} \tag{A.10}$$

$$F_{13} = -A_N^B(\hat{q}) \left.\frac{\partial \boldsymbol{\omega}_{N/I}^N}{\partial \boldsymbol{v}^N}\right|_{\hat{\boldsymbol{p}}} \tag{A.11}$$

$$F_{16} = -\left(diag(\tilde{\boldsymbol{\omega}}_{B/I}^B) - diag(\hat{\boldsymbol{\beta}}_g)\right) \tag{A.12}$$

$$F_{22} = \left.\frac{\partial \dot{\boldsymbol{p}}}{\partial \boldsymbol{p}}\right|_{\hat{\boldsymbol{p}}, \hat{\boldsymbol{v}}^N} \tag{A.13}$$

$$F_{23} = \left.\frac{\partial \dot{\boldsymbol{p}}}{\partial \boldsymbol{v}^N}\right|_{\hat{\boldsymbol{p}}} \tag{A.14}$$

$$F_{31} = -A_B^N(\hat{q})[\hat{\boldsymbol{a}}^B \times] \tag{A.15}$$

$$F_{32} = \left.\frac{\partial \dot{\boldsymbol{v}}^N}{\partial \boldsymbol{p}}\right|_{\hat{\boldsymbol{p}}, \hat{\boldsymbol{v}}^N} \tag{A.16}$$

$$F_{33} = \left.\frac{\partial \dot{\boldsymbol{v}}^N}{\partial \boldsymbol{v}^N}\right|_{\hat{\boldsymbol{p}}, \hat{\boldsymbol{v}}^N} \tag{A.17}$$

$$F_{31} = -A_B^N(\hat{q})[\hat{\boldsymbol{a}}^B \times] \tag{A.18}$$

$$F_{35} = -A_B^N(\hat{q}) \tag{A.19}$$

$$F_{35} = -A_B^N(\hat{q})\left(diag(\tilde{\boldsymbol{a}}^B) - diag(\hat{\beta}_a)\right) \tag{A.20}$$

The angular rate partials are given by

$$\frac{\partial \boldsymbol{\omega}_{N/I}^N}{\partial \boldsymbol{p}} = \begin{bmatrix} -\omega_m \sin\phi & 0 & -\dfrac{v_E}{R_m^2} \\ 0 & 0 & \dfrac{v_N}{R_m^2} \\ -\omega_m \cos\phi - \dfrac{v_E \sec^2\phi}{R_m} & 0 & \dfrac{v_E \tan\phi}{R_m^2} \end{bmatrix} \tag{A.21}$$

$$\frac{\partial \boldsymbol{\omega}_{N/I}^N}{\partial \boldsymbol{v}^N} = \begin{bmatrix} 0 & \dfrac{1}{R_m} & 0 \\[2ex] -\dfrac{1}{R_m} & 0 & 0 \\[2ex] 0 & -\dfrac{\tan\phi}{R_m} & 0 \end{bmatrix} \tag{A.22}$$

The position partials are given by

$$\frac{\partial \dot{\boldsymbol{p}}}{\partial \boldsymbol{p}} = \begin{bmatrix} 0 & 0 & -\dfrac{v_N}{R_m^2} \\[2ex] \dfrac{v_E \sec\phi \tan\phi}{R_m} & 0 & -\dfrac{v_E \sec\phi}{R_m^2} \\[2ex] 0 & 0 & 0 \end{bmatrix} \tag{A.23}$$

$$\frac{\partial \dot{\boldsymbol{p}}}{\partial \boldsymbol{v}^N} = \begin{bmatrix} \dfrac{1}{R_m} & 0 & 0 \\[2ex] 0 & \dfrac{\sec\phi}{R_m} & 0 \\[2ex] 0 & 0 & -1 \end{bmatrix} \tag{A.24}$$

The velocity partials are given by

$$\frac{\partial \dot{\boldsymbol{v}}^N}{\partial \boldsymbol{p}} = \begin{bmatrix} Y_{11} & 0 & Y_{13} \\ Y_{21} & 0 & Y_{23} \\ Y_{31} & 0 & Y_{33} \end{bmatrix} \tag{A.25}$$

$$Y_{11} = -2\omega_m v_E \cos\phi - \frac{v_E^2 \sec^2\phi}{R_m} \tag{A.26}$$

$$Y_{13} = \frac{v_E^2 \tan\phi}{R_m^2} - \frac{v_N v_D}{R_m^2} \tag{A.27}$$

$$Y_{21} = 2\omega_m v_N \cos\phi - 2\omega_m v_D \sin\phi + \frac{v_E v_N \sec^2\phi}{R_m} \tag{A.28}$$

$$Y_{23} = -v_E \left[ \frac{v_N \tan\phi + v_D}{R_m^2} \right] \tag{A.29}$$

$$Y_{31} = 2\omega_m v_D \sin\phi + \frac{\partial g}{\partial \phi} \tag{A.30}$$

$$Y_{33} = \frac{v_E^2}{R_m^2} + \frac{v_N^2}{R_m^2} + \frac{\partial g}{\partial h} \tag{A.31}$$

$$\frac{\partial \dot{\boldsymbol{v}}^N}{\partial \boldsymbol{v}^N} = \begin{bmatrix} \dfrac{v_D}{R_m} & \omega_m \sin\phi - \dfrac{2v_E \tan\phi}{R_m} & \dfrac{v_N}{R_m} \\[3ex] 2\omega_m \sin\phi + \dfrac{v_E \tan\phi}{R_m} & \dfrac{v_D + v_N \tan\phi}{R_m} & 2\omega_m \cos\phi + \dfrac{v_E}{R_m} \\[3ex] -\dfrac{2v_N}{R_m} & -2\omega_m \cos\phi - \dfrac{2v_E}{R_m} & 0 \end{bmatrix} \quad \text{(A.32)}$$

APPENDIX B:

COORDINATE SYSTEMS

Coordinate systems used in this thesis are defined in this appendix.

Body Frame (B) - The center of the body frame is located at the center of gravity of the vehicle. The X-axis points in the direction of the front of the vehicle. The z-axis points in the direction of the bottom of the vehicle. The Y-axis completes the right-handed system.

Earth Centered Inertial (ECI) - The Z-axis points in the direction of the North pole. The X-axis points in the direction of the vernal equinox through the equatorial plane. The Y-axis completes the right-handed system.

Earth Centered-Earth Fixed (ECEF) - The Z-axis points in the direction of the North pole. The X-axis points in the direction of the prime meridian in the equatorial plane. The Y-axis completes the right-handed system.

Moon Centered-Moon Fixed (MCMF) - Similar to the Z-axis points in the direction of the Moon's North pole. The X-axis points in the direction of the Moon's prime meridian in the equatorial plane. The Y-axis completes the right-handed system.

North East Down (NED) - This reference frame is local to the object's position and is formed to a tangent plane to the object's reference ellipsoid. The North-axis points in the direction of true North. The East-axis points in the East direction. The Down-direction completes the right-handed system and points in the direction of the center of the planetary object.

APPENDIX C:

SECOND ELLIPTICAL ORBIT DATA (315X200 KM)

The following plots are filter output for the second tracking pass of the elliptical 315x200 km orbit.
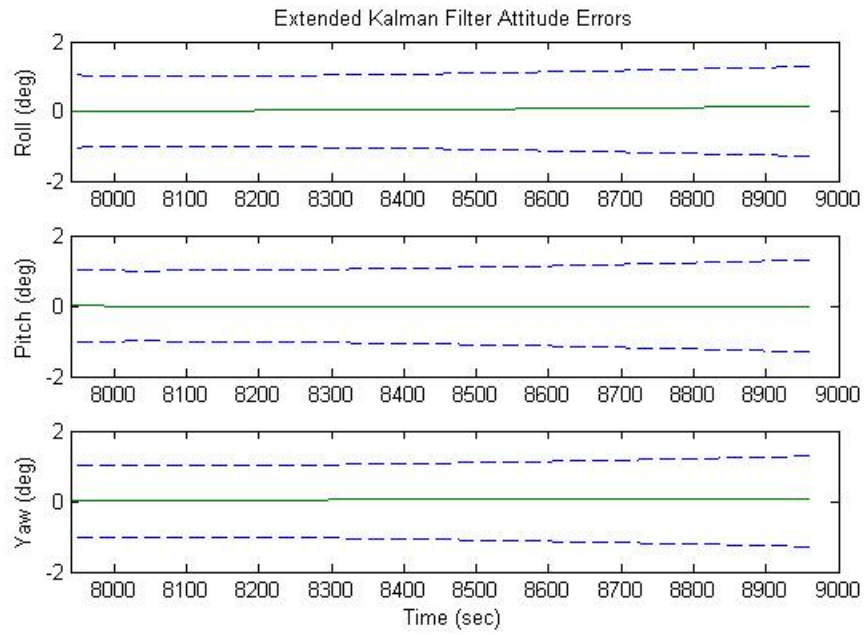


Figure C-1 Elliptical Orbit 2 EKF Attitude Error
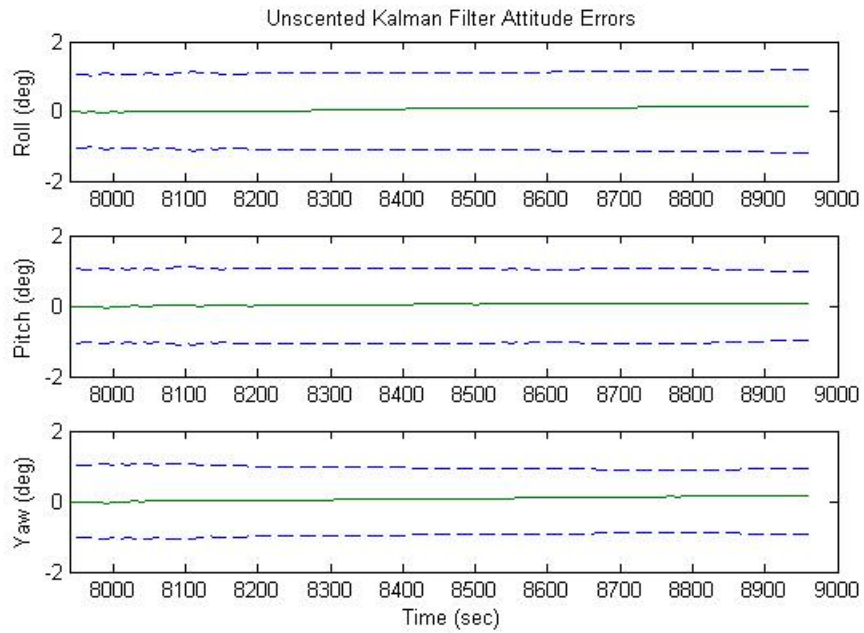
Figure C-2 Elliptical Orbit 2 UKF Attitude Error
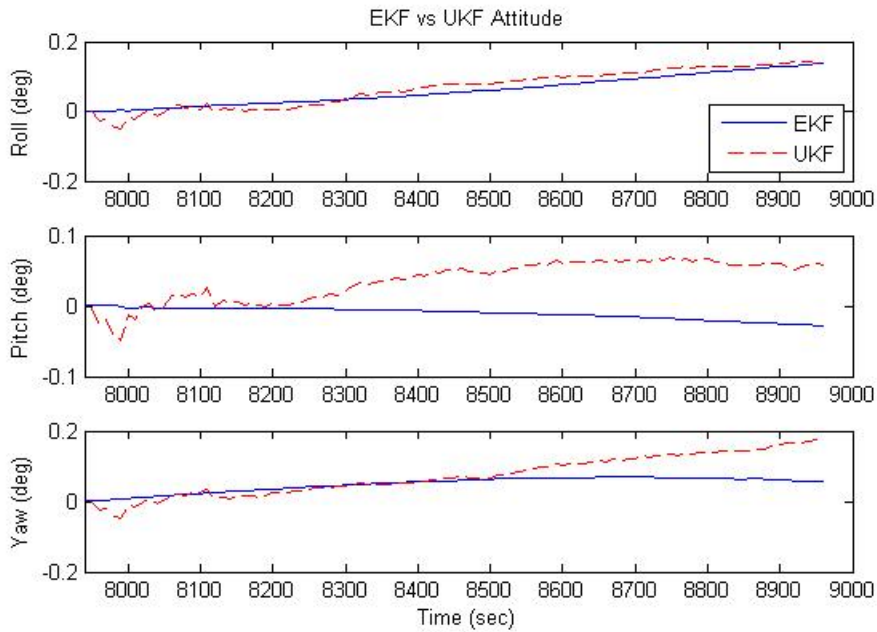


Figure C-3 Elliptical Orbit 2 EKF vs UKF Attitude Error
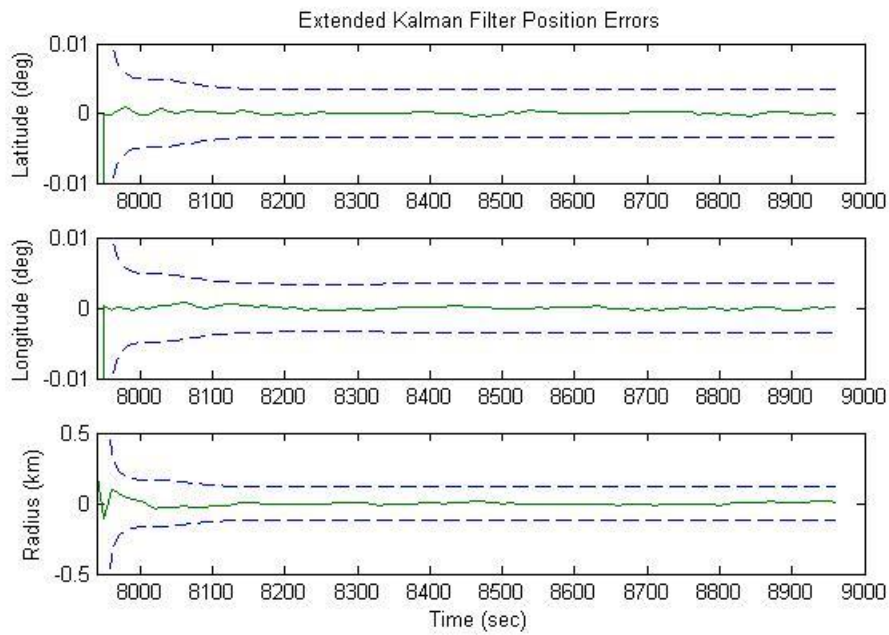
Figure C-4 Elliptical Orbit 2 EKF Position Error
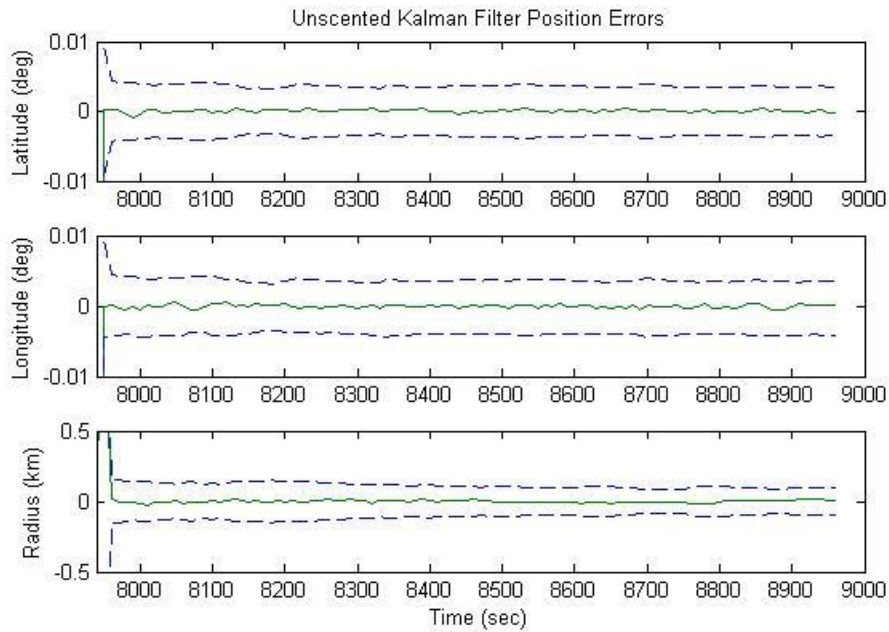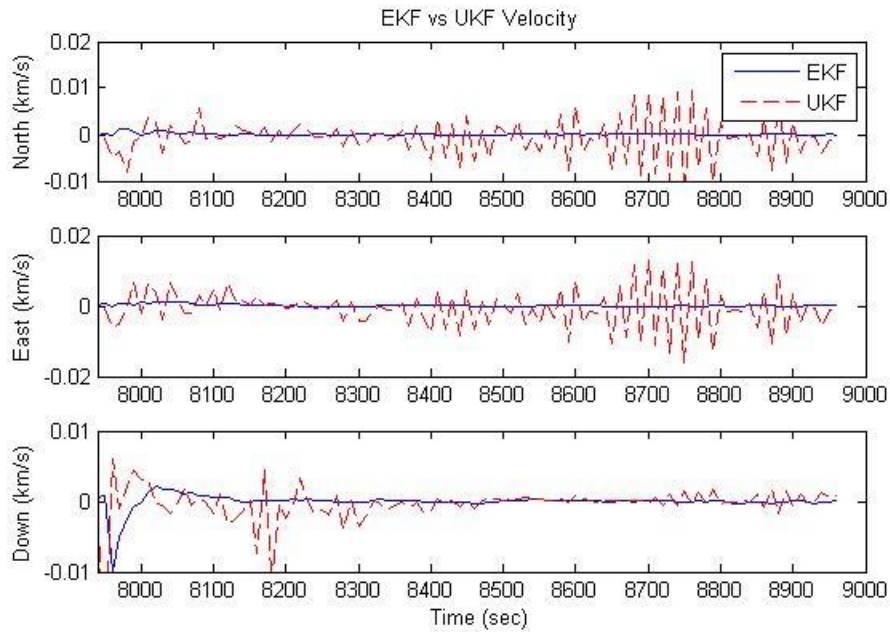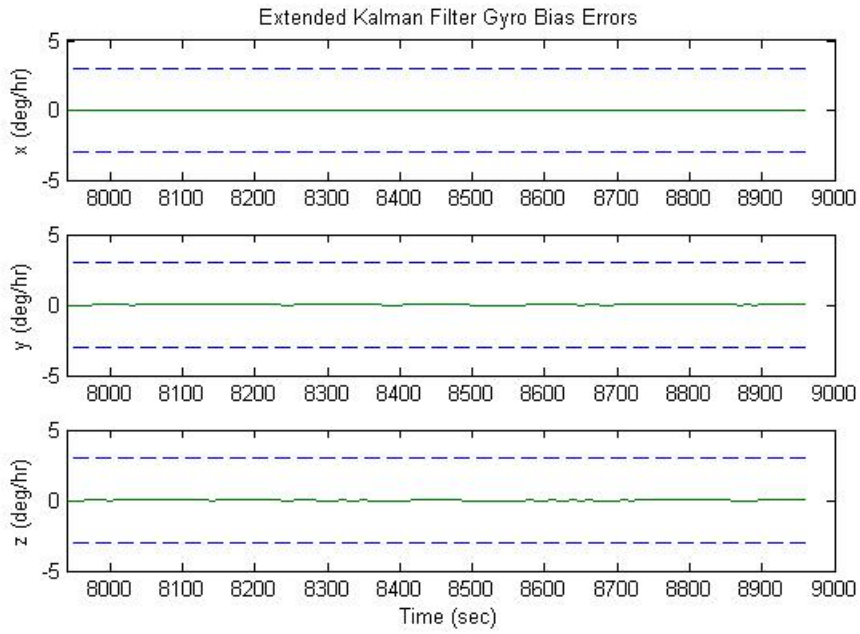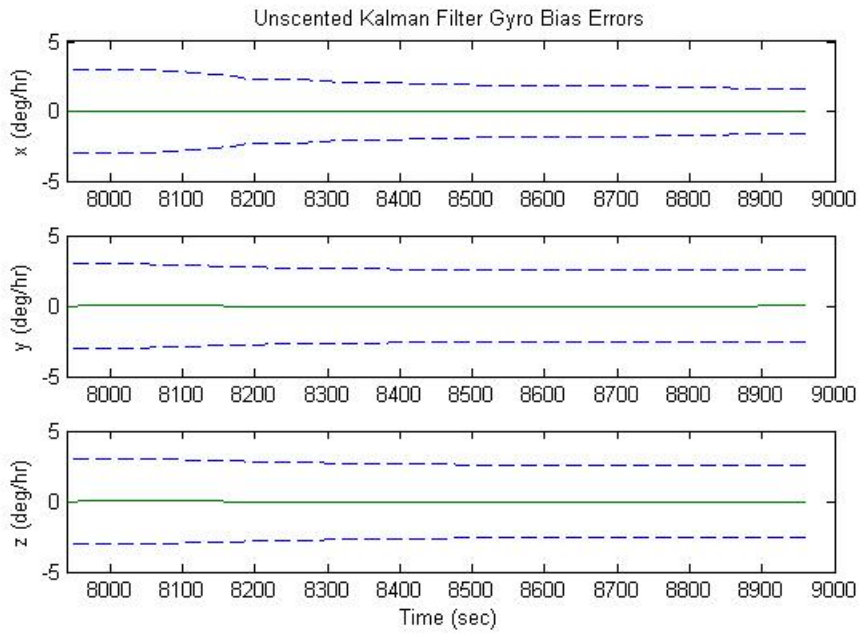


Figure C-5 Elliptical Orbit 2 UKF Position Error
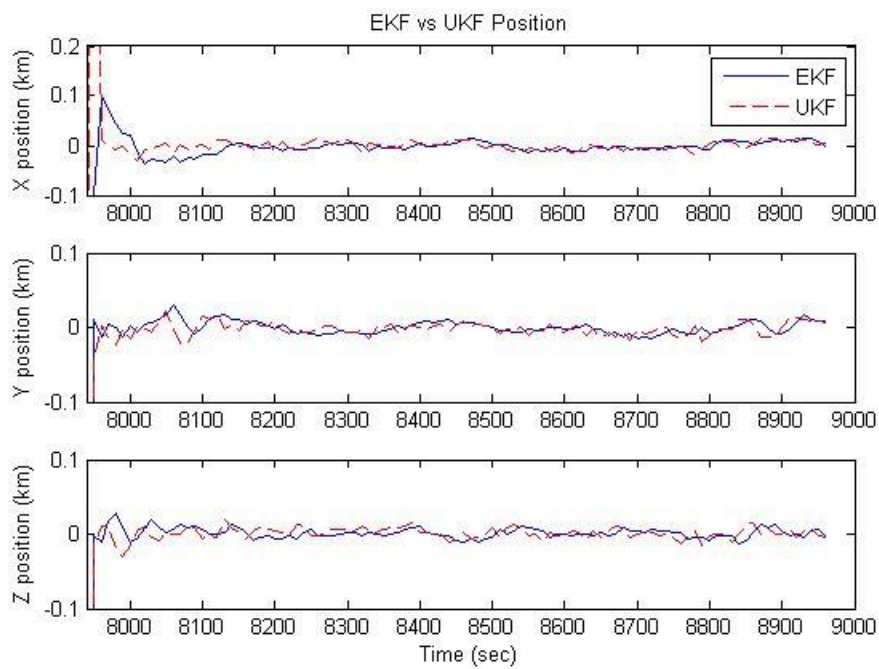
Figure C-6 Elliptical Orbit 2 EKF vs UKF Position Error
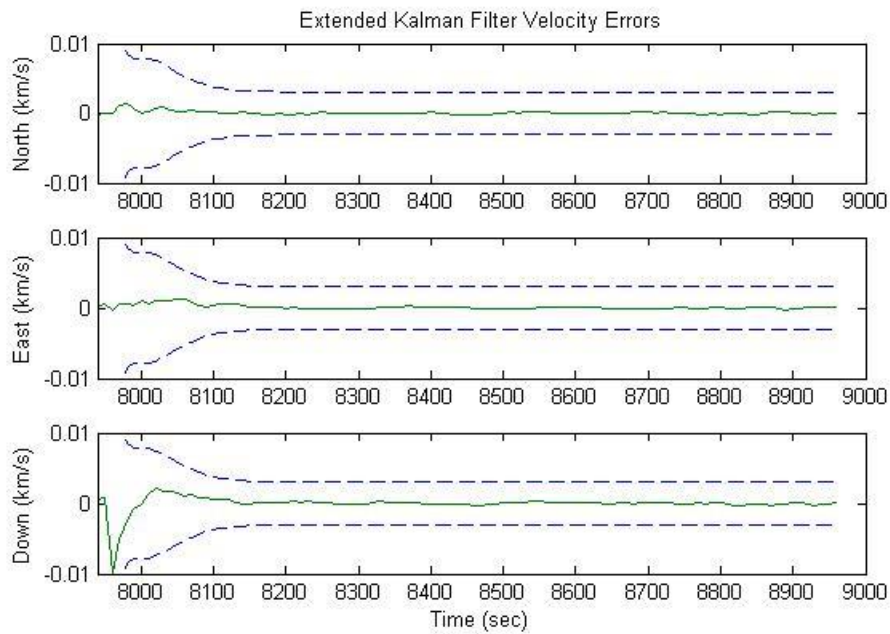


Figure C-7 Elliptical Orbit 2 EKF Velocity Error
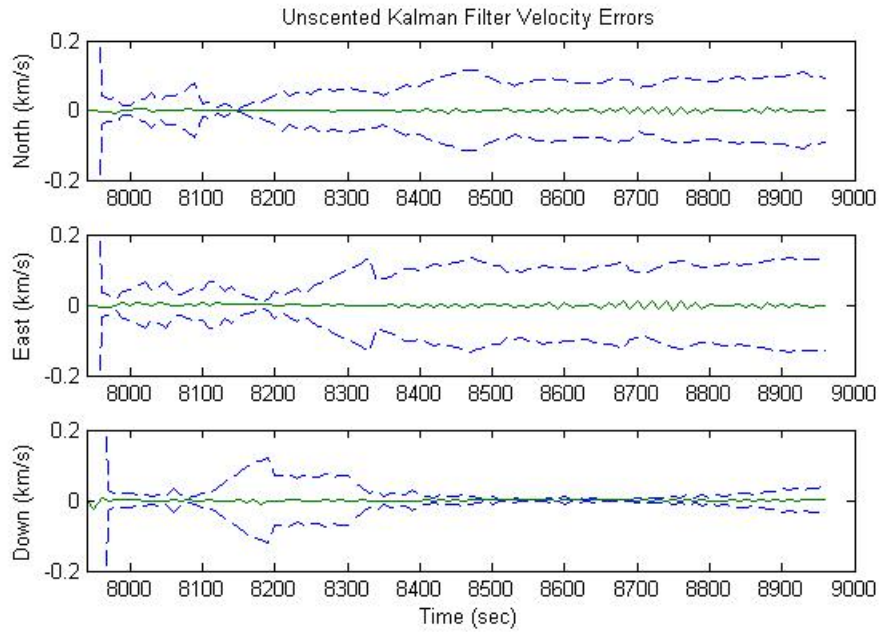
Figure C-8 Elliptical Orbit 2 UKF Velocity Error



Figure C-9 Elliptical Orbit 2 EKF vs UKF Velocity Error

54

Figure C-10 MC1 Elliptical Orbit 2 EKF Gyro Bias



Figure C-11 Elliptical Orbit 2 UKF Gyro Bias
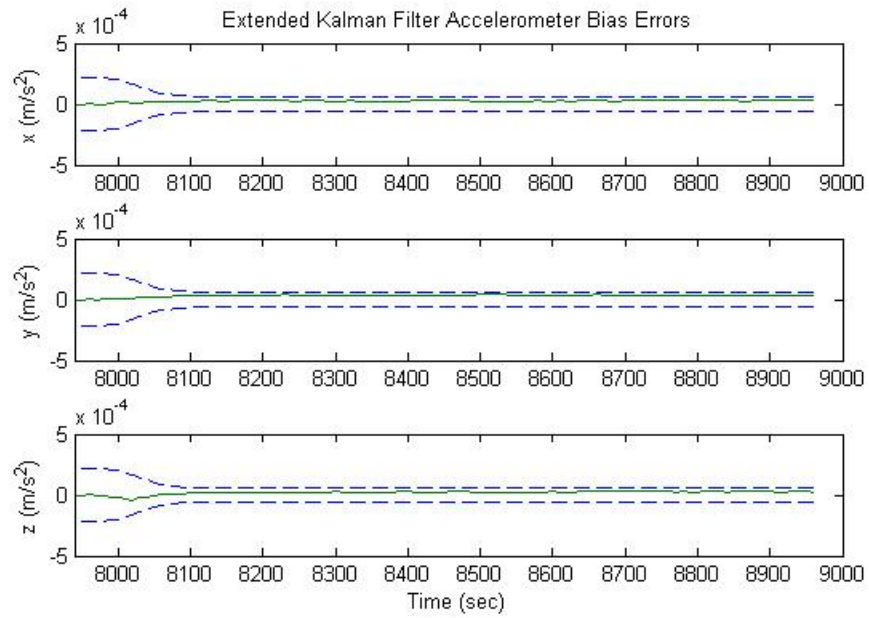
Figure C-12 Elliptical Orbit 2 EKF Accelerometer Bias
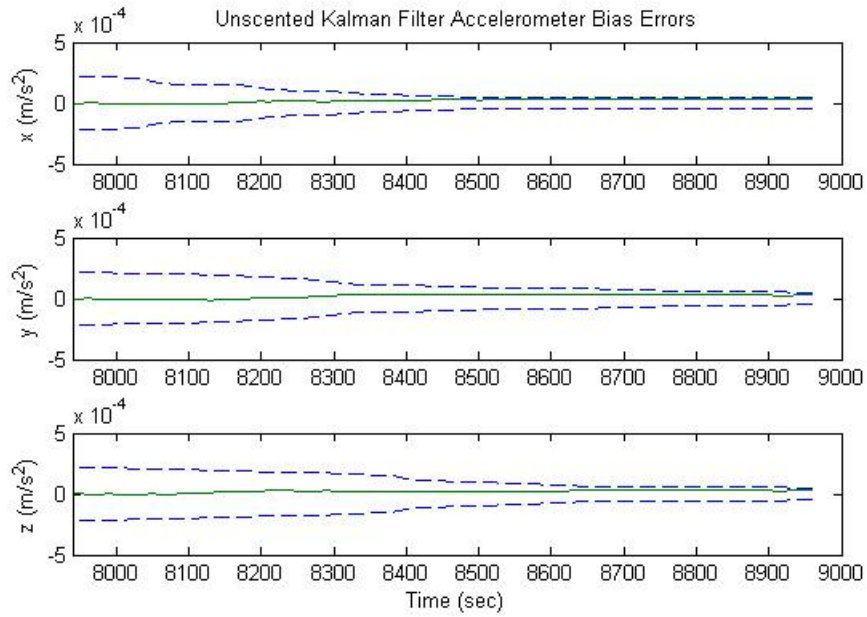


Figure C-13 Elliptical Orbit 2 UKF Accelerometer Bias

APPENDIX D:

FIRST CIRCULAR ORBIT DATA (200X200 KM)

The following plots are filter output for the first tracking pass of the circular 200x200 km orbit.
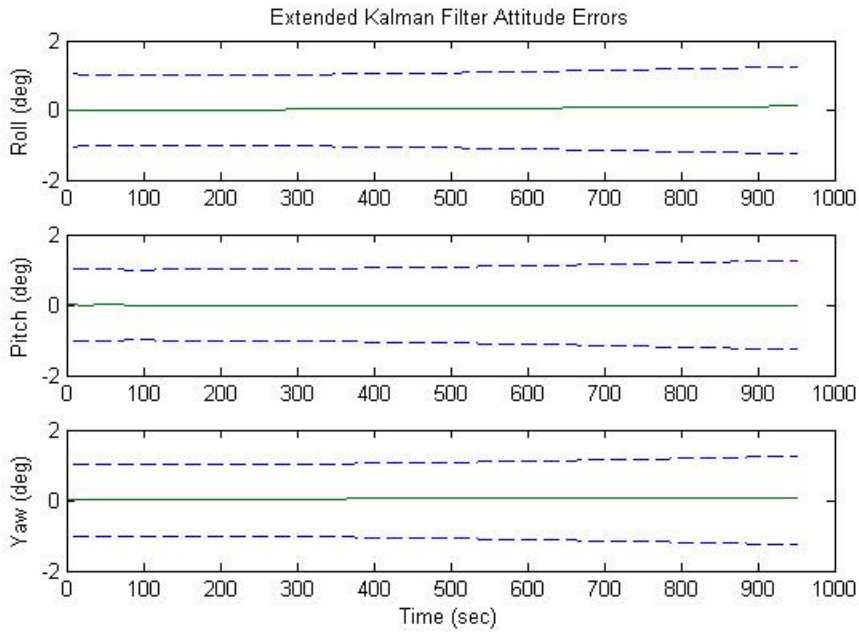


Figure D-1 Circular Orbit 1 EKF Attitude Error
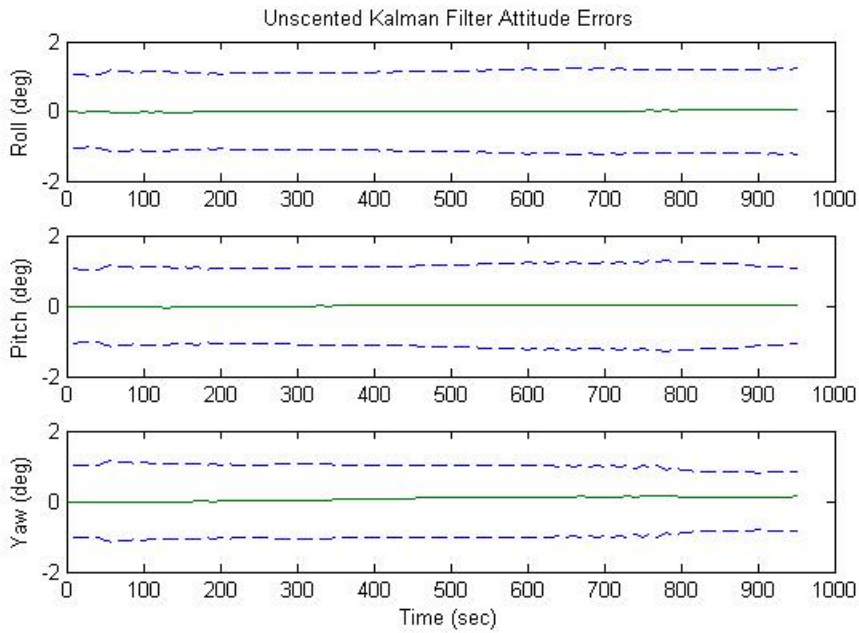


Figure D-2 Circular Orbit 1 UKF Attitude Error
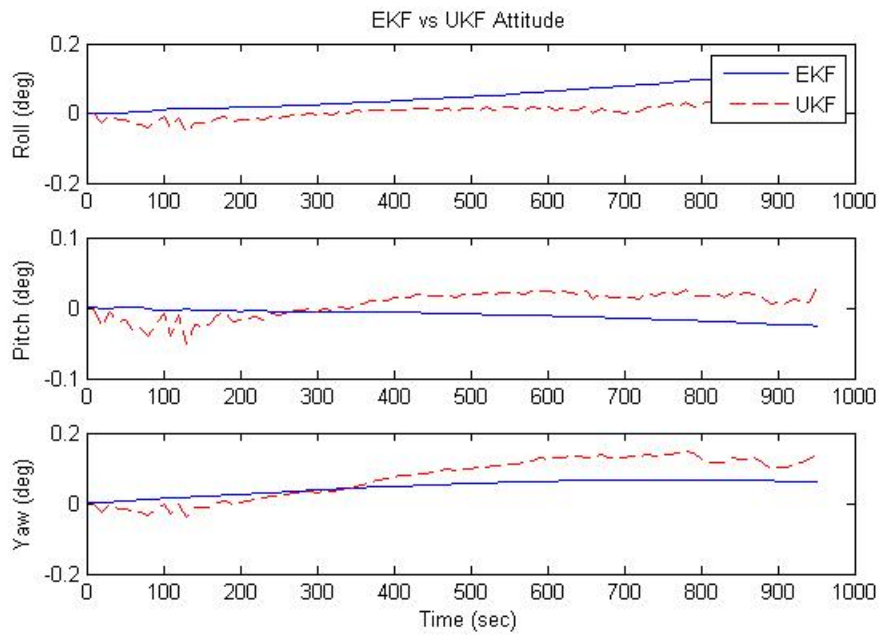
Figure D-3 Circular Orbit 1 EKF vs UKF Attitude Error
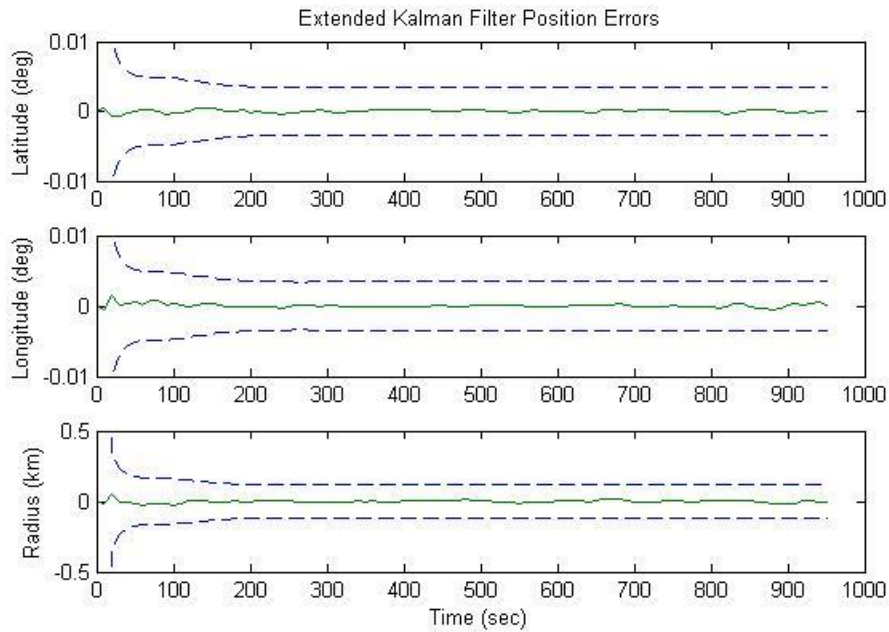


Figure D-4 Circular Orbit 1 EKF Position Error
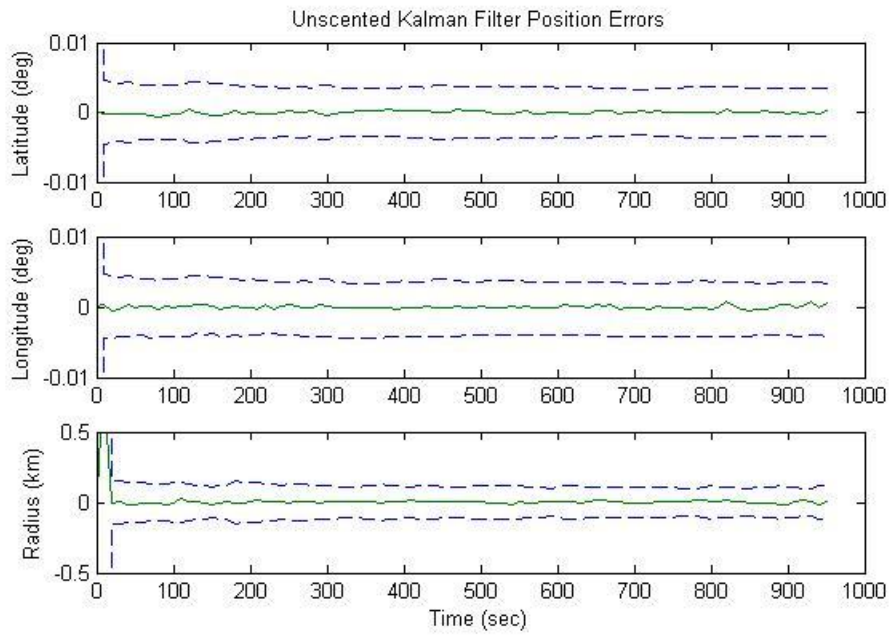
Figure D-5 Circular Orbit 1 UKF Position Error
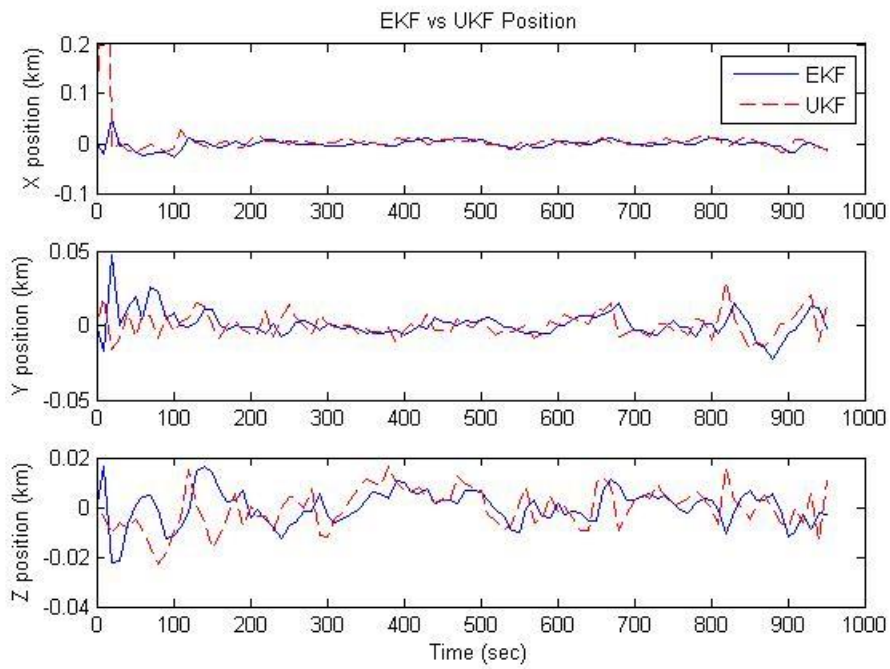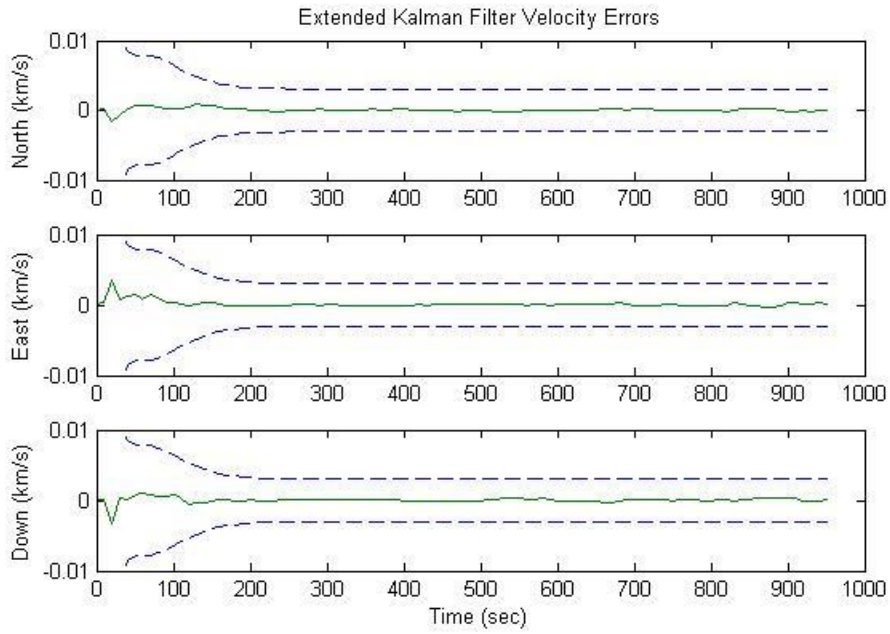


Figure D-6 Circular Orbit 1 EKF vs UKF Position Error
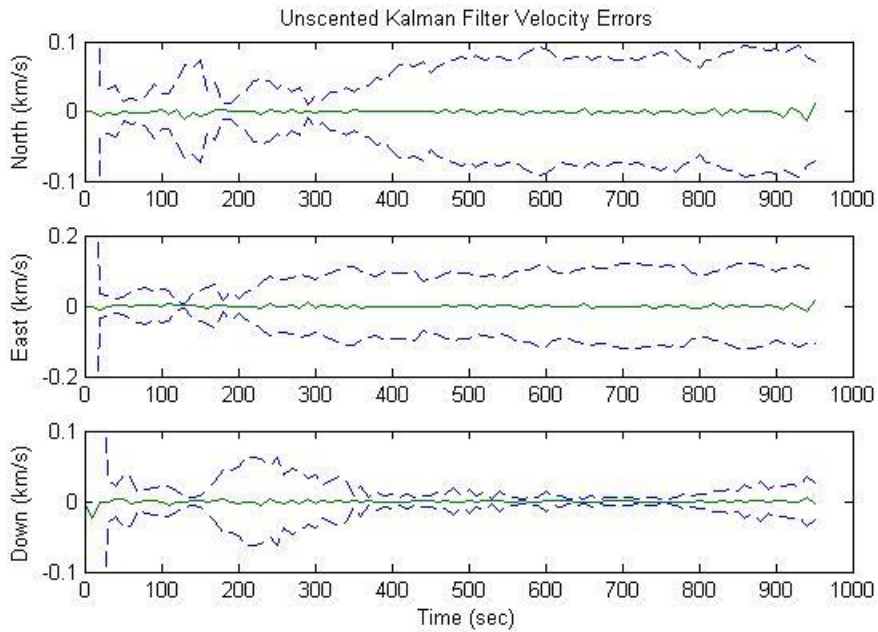
Figure D-7 Circular Orbit 1 EKF Velocity Error
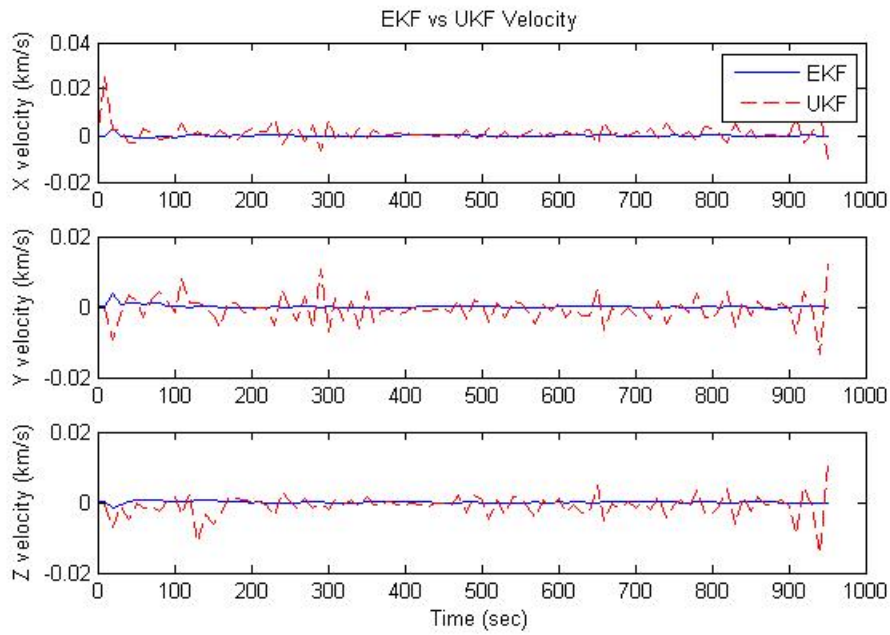


Figure D-8 Circular Orbit 1 UKF Velocity Error

Figure D-9 Circular Orbit 1 EKF vs UKFVelocity Error
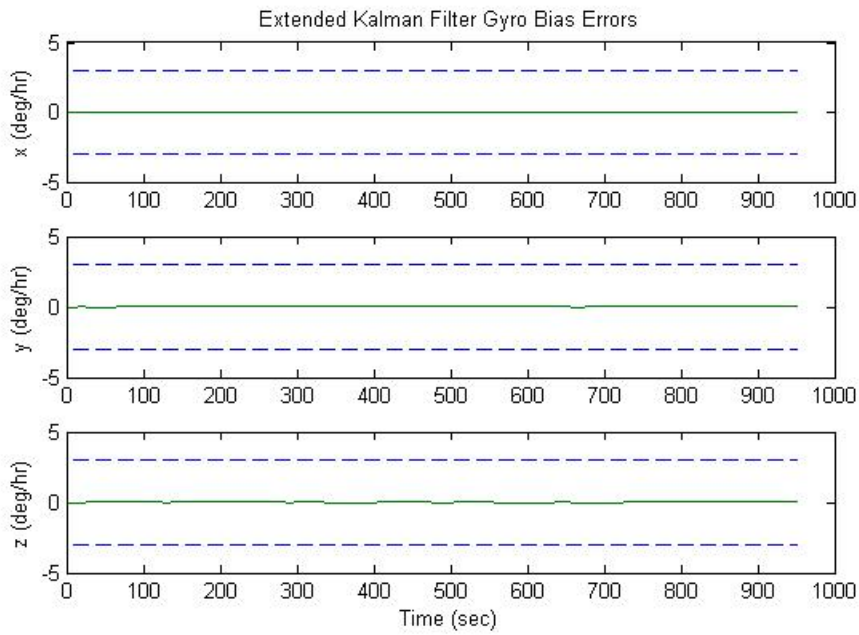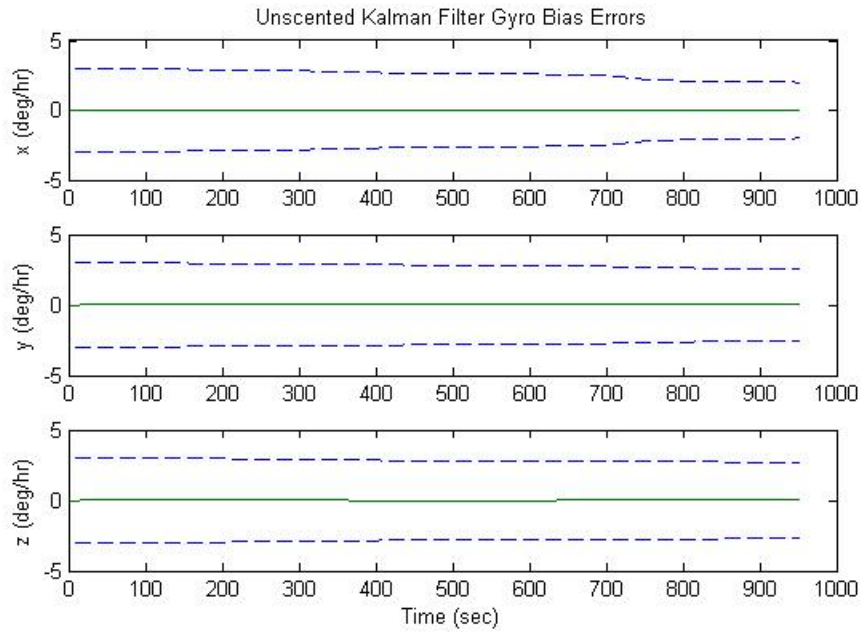


Figure D-10 Circular Orbit 1 EKF Gyro Bias

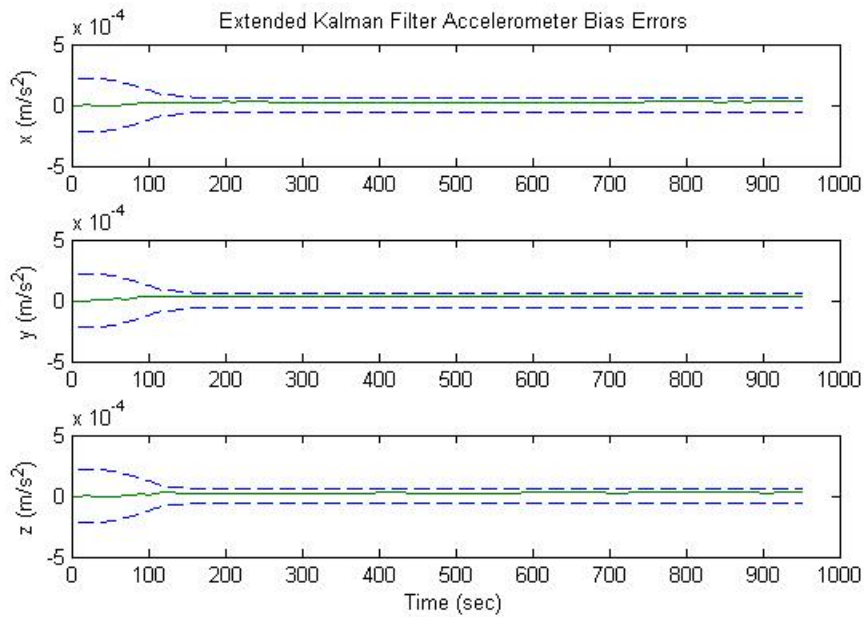Figure D-11 Circular Orbit 1 UKF Gyro Bias



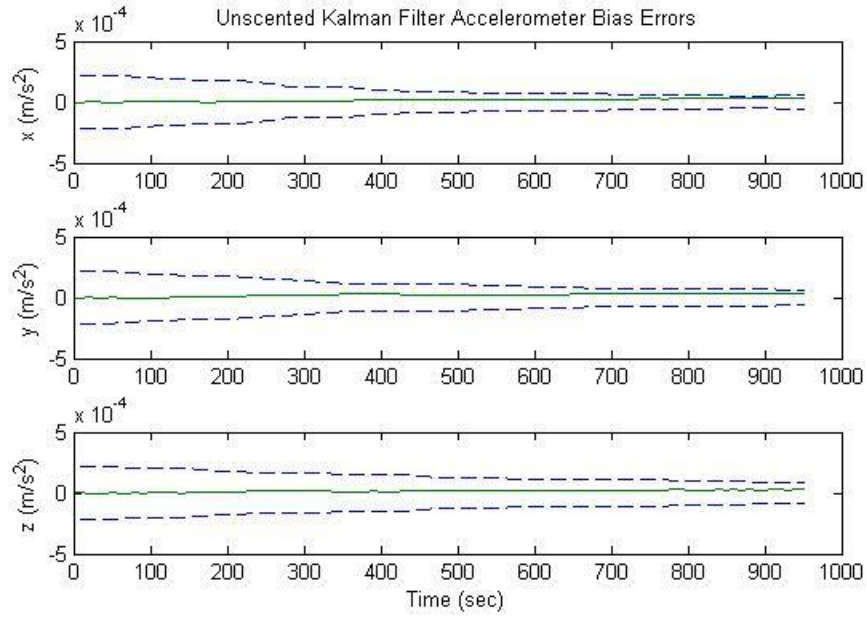Figure D-12 Circular Orbit 1 EKF Accelerometer Bias

Figure D-13 Circular Orbit 1 UKF Accelerometer Bias

APPENDIX E:

SECOND CIRCULAR ORBIT DATA (200X200 KM)

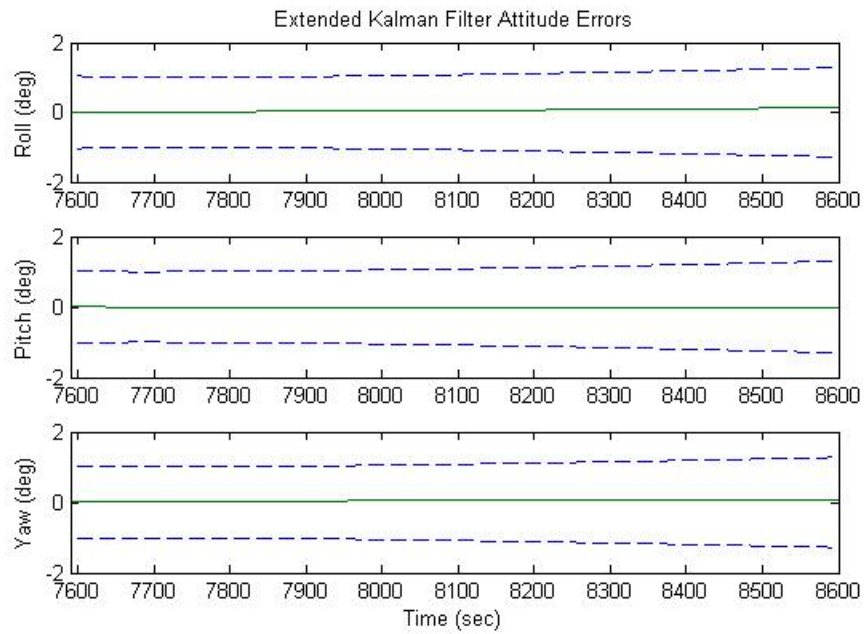The following plots are filter output for the second tracking pass of the circular 200x200 km orbit.



Figure E-1 Circular Orbit 2 EKF Attitude Error

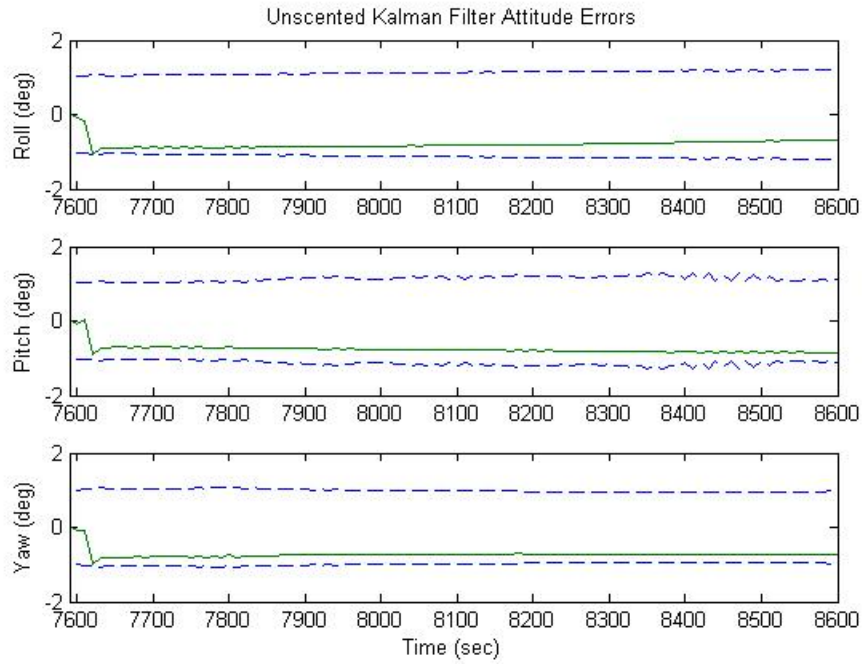Figure E-2 Circular Orbit 2 UKF Attitude Error
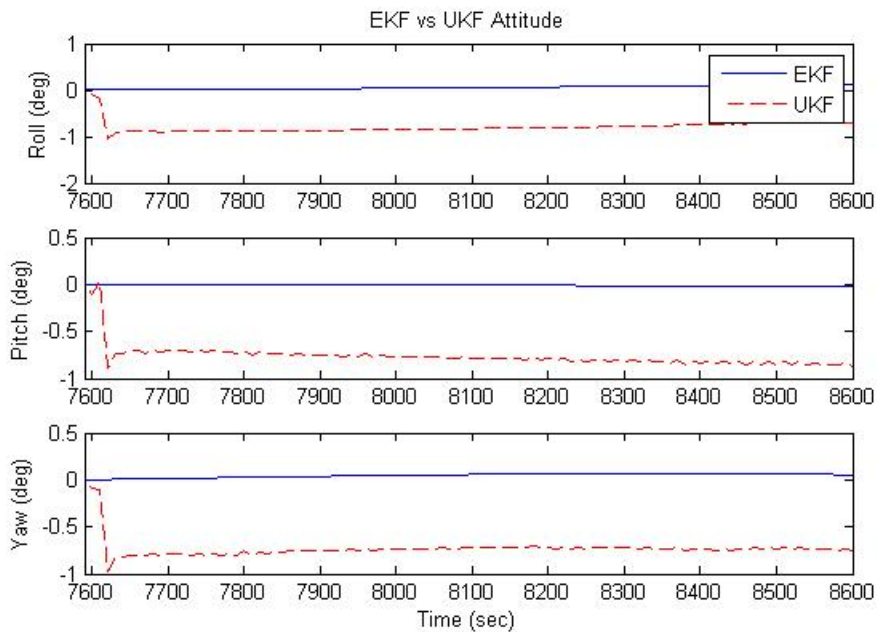


Figure E-3 Circular Orbit 2 EKF vs UKF Attitude Error

67

Figure E-4 Circular Orbit 2 EKF Position Error



Figure E-5 Circular Orbit 2 UKF Position Error

Figure E-6 Circular Orbit 2 EKF vs UKF Position Error



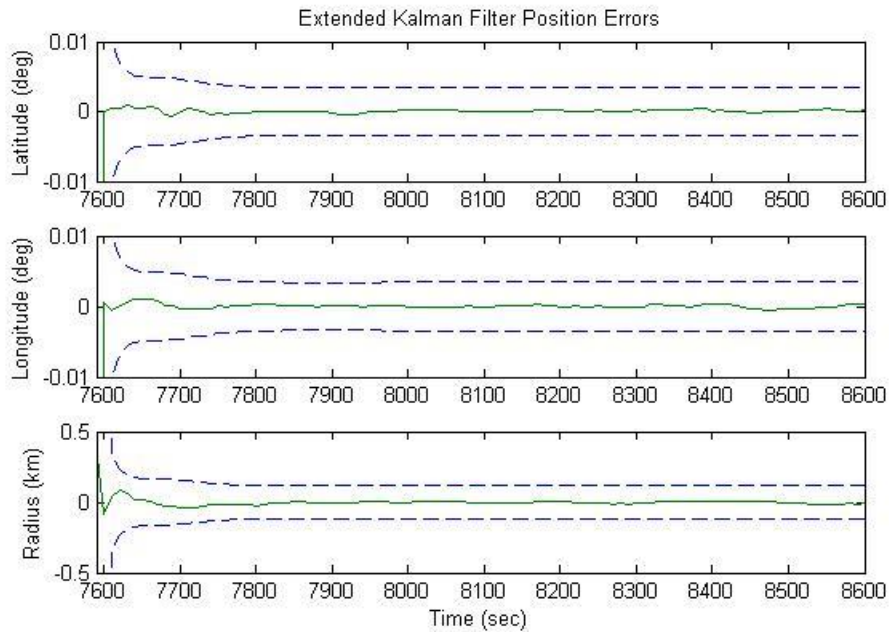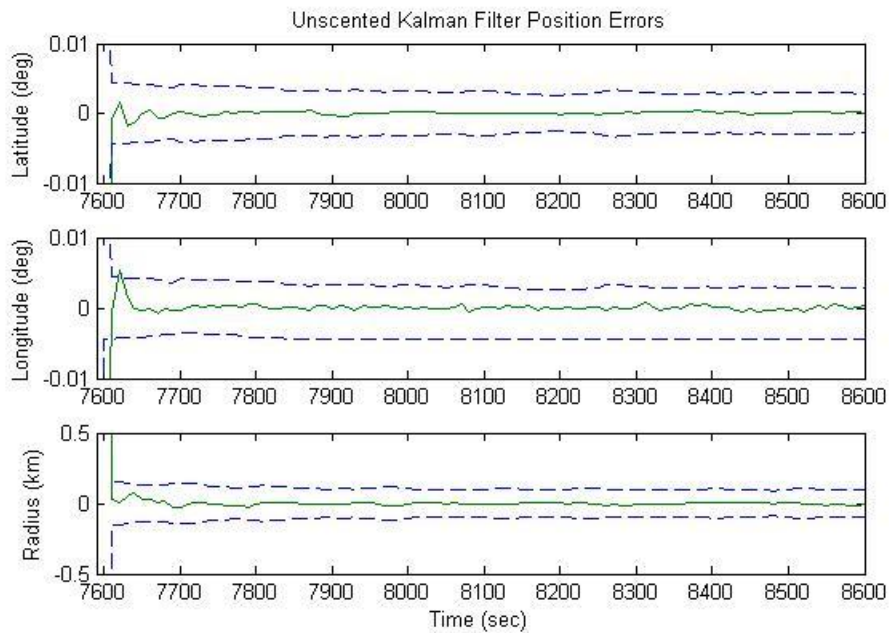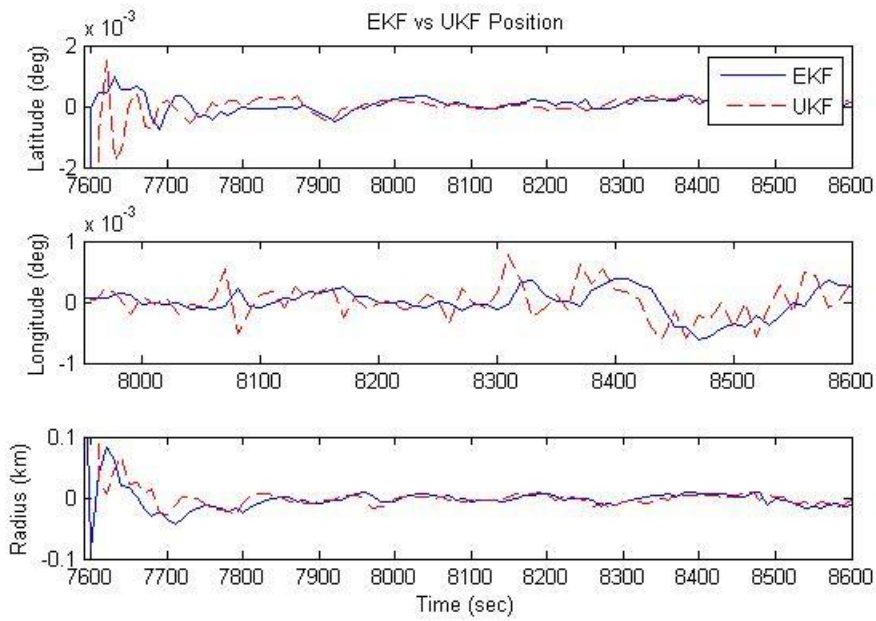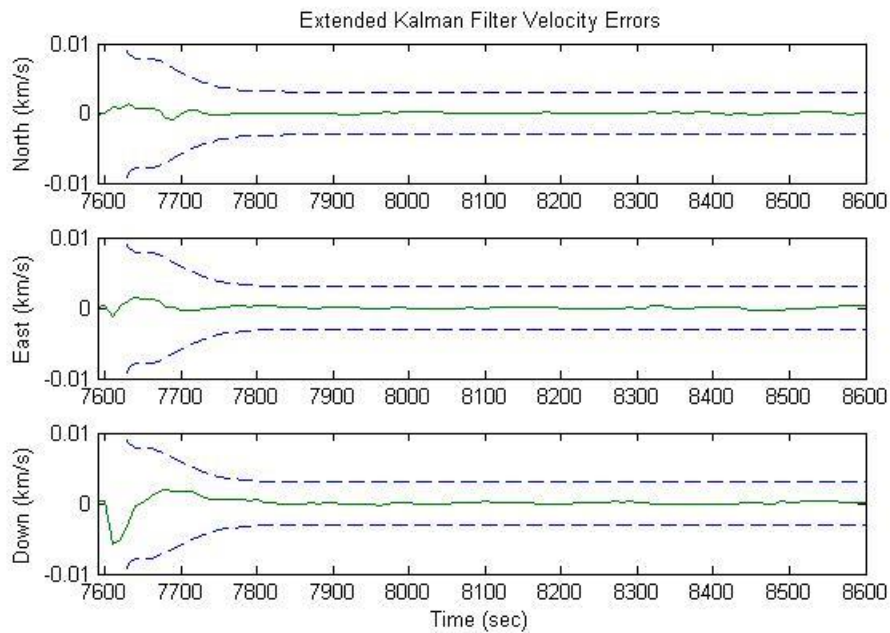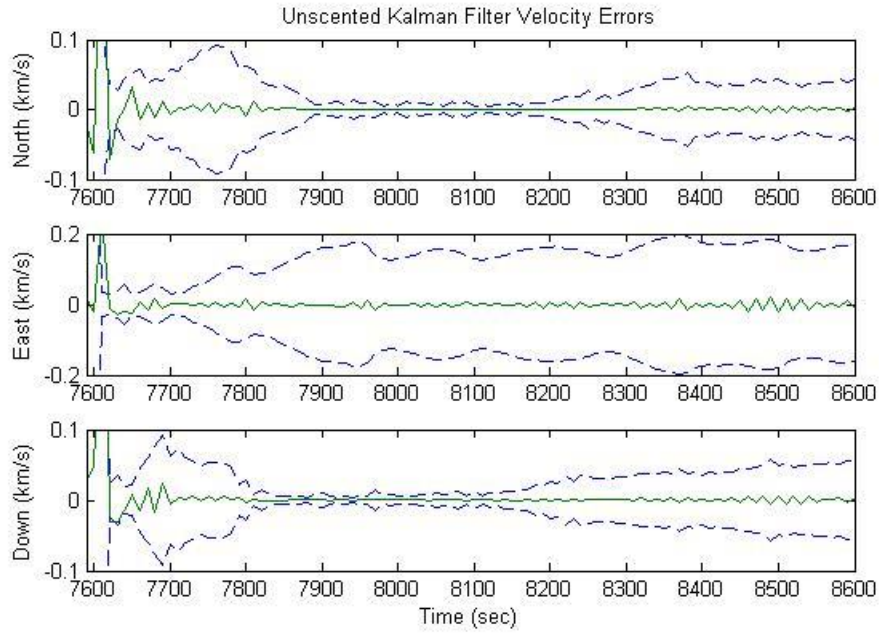Figure E-7 Circular Orbit 2 EKF Velocity Error

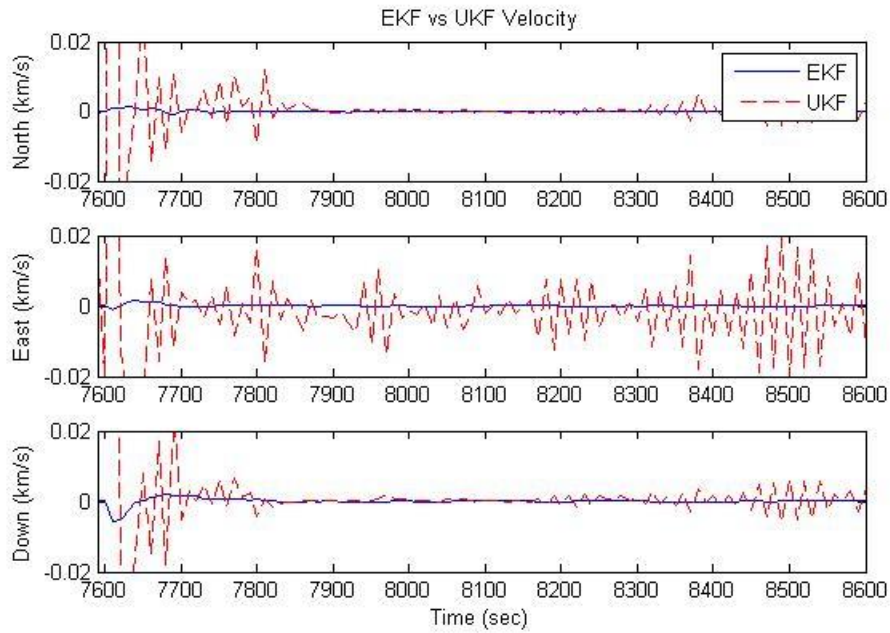Figure E-8 Circular Orbit 2 UKF Velocity Error



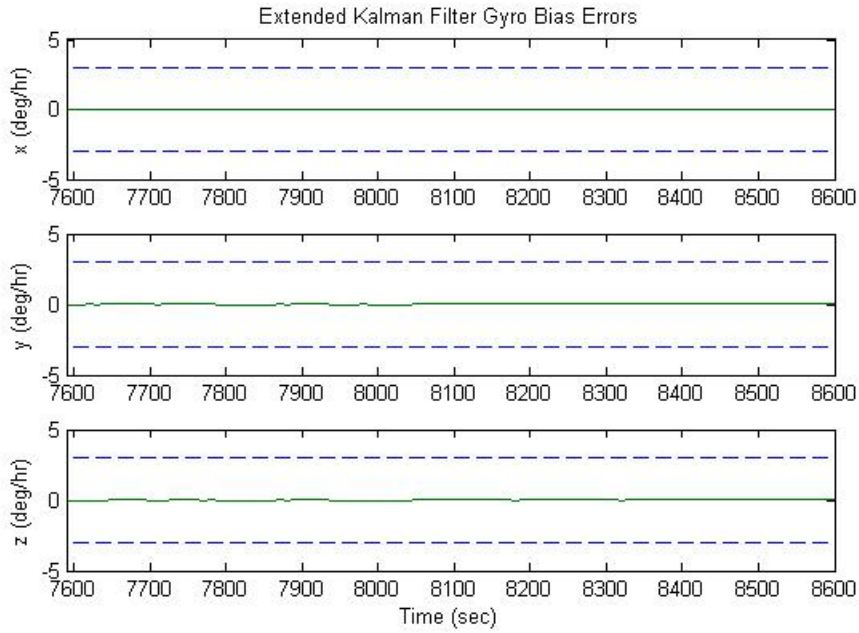Figure E-9 Circular Orbit 2 EKF vs UKF Velocity Error
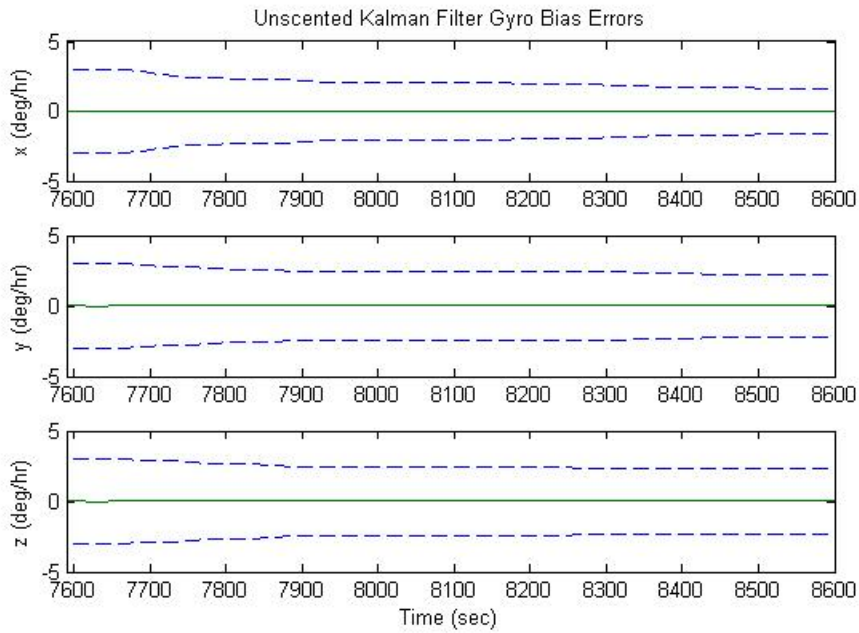
Figure E-10 Circular Orbit 2 EKF Gyro Bias



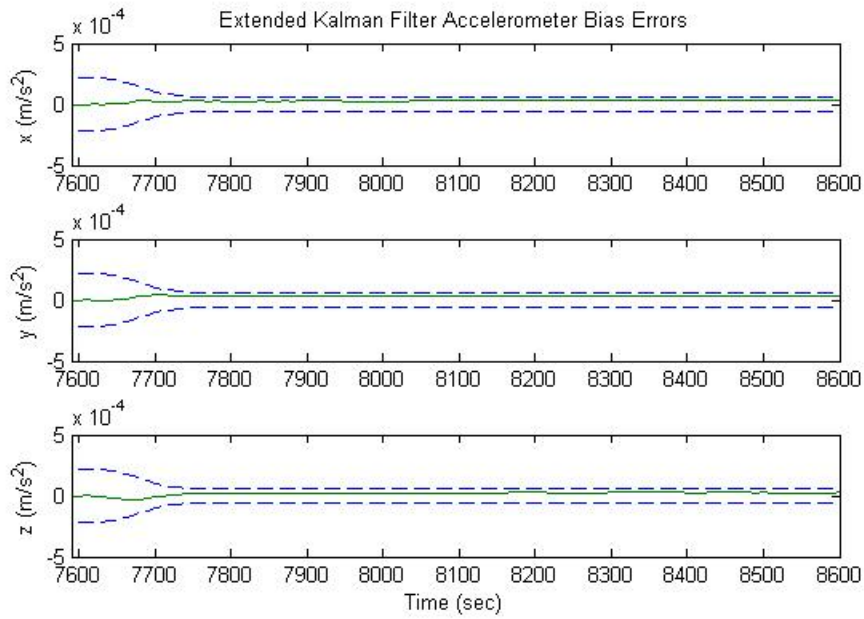Figure E-11 Circular Orbit 2 UKF Gyro Bias
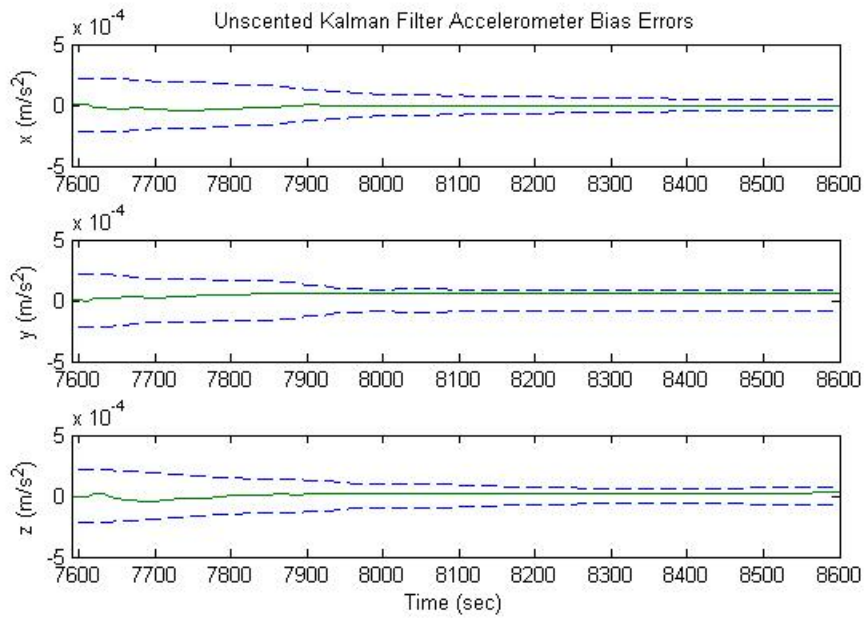
Figure E-12 Circular Orbit 2 EKF Accelerometer Bias



Figure E-13 Elliptical Orbit 2 UKF Accelerometer Bias

APPENDIX F:

RAO-BLACKWELLIZED PARTICLE FILTER

Particle filters are another method to approximate a nonlinear system. The particle filter seeks to provide an accurate representation of the posterior probability distribution function. The filter propagates a large number of particles that are randomly sampled and weights them using a likelihood function to determine which particles closely match the measurements. The particles will that are weighted more allows for the filter to provide a more accurate approximation of the estimate compared to the truth. The performance of the filter depends the sampling of the particles. Particle filters tend to suffer from particle degeneracy because the samples are more than likely outside the significant region of the state space. The method for sampling of the particles plays an important role in how well the filter will perform.

Sampling of all elements of a state leads to a high computational cost due to the large number of particles that are propagated. A method has been developed using the Rao-Blackwell theorem that can reduce these computations. The system state can be partitioned into nonlinear and conditionally linear parts. This is called the Rao-Blackwellized Particle Filter (RBPF). The RBPF treats a part of the system as conditionally linear, which allows for the estimate to be determined by a Kalman filter or extended Kalman filter. This arrangement is convenient for navigation systems. The RBPF can apply a particle filter to the position state and the conditional linearity to the velocity state. The same will hold true with the attitude state being considered as conditionally linear. This reduces the amount of sampling data points compared to a particle filter, which reduces computational time.

The RBPF uses the following equations for the partitioned state.

$$x_{1k+1} = f(x_{1k}) + \Phi_{1k} x_{2k} + \Upsilon_{1k} w_{1k} \tag{F.1}$$

$$x_{2k+1} = \Phi_{2k} x_{2k} + \Upsilon_{2k} w_{2k} \tag{F.2}$$

$$\tilde{y}_k = h(x_{1k}) + v_k \tag{F.3}$$

where $x_{1k} = [\phi \ \lambda \ r]$ and $x_{2k} = [\varrho \ v_N \ v_E \ v_D \ \boldsymbol{\beta}_g \ \boldsymbol{\beta}_a]$. The matrices $\boldsymbol{\Phi}_{1k}$ and $\boldsymbol{\Phi}_{2k}$ will be propagation matrices following the previous defined equations of motion. The process noise variables $\boldsymbol{w}_{1k}$ and $\boldsymbol{w}_{2k}$ are assumed to be zero mean Guassian noise processes represented as

$$\begin{bmatrix} w_{1k} \\ w_{2k} \end{bmatrix} \sim N \left( \begin{bmatrix} \mathbf{0} \\ \mathbf{0} \end{bmatrix}, \begin{bmatrix} Q_{1k} & Q_{12k} \\ Q_{12k}^T & Q_{2k} \end{bmatrix} \right) \tag{F.4}$$

However, $\boldsymbol{w}_{1k}, Q_{1k}$ and $Q_{12k}$ are zero for this application. The process noise vector, $\boldsymbol{w}_{2k}$, and covariance, $Q_{2k}$, are defined as

$$w_{2k} = \begin{bmatrix} \eta_{gv} \\ \eta_{gu} \\ \eta_{av} \\ \eta_{au} \end{bmatrix} \tag{F.5}$$

$$Q_{2k} = \begin{bmatrix} \sigma_{gv}^2 I_{3\times3} & 0_{3\times3} & 0_{3\times3} & 0_{3\times3} \\ 0_{3\times3} & \sigma_{gu}^2 I_{3\times3} & 0_{3\times3} & 0_{3\times3} \\ 0_{3\times3} & 0_{3\times3} & \sigma_{av}^2 I_{3\times3} & 0_{3\times3} \\ 0_{3\times3} & 0_{3\times3} & 0_{3\times3} & \sigma_{au}^2 I_{3\times3} \end{bmatrix} \tag{F.6}$$

and the corresponding matrix transform to the $x_2$ navigation state described in the RBPF algorithm is

$$\Upsilon_{2k} = \begin{bmatrix} -I_{3\times3} & 0_{3\times3} & 0_{3\times3} & 0_{3\times3} \\ 0_{3\times3} & 0_{3\times3} & -A_B^N(\widehat{q})I_{3\times3} & 0_{3\times3} \\ 0_{3\times3} & 0_{3\times3} & 0_{3\times3} & 0_{3\times3} \\ 0_{3\times3} & 0_{3\times3} & 0_{3\times3} & 0_{3\times3} \end{bmatrix} \tag{F.7}$$

The algorithm for the RBPF is as follows and can be found in both Crassidis [5] and Nordlund [10]. The first part consists of initialization by generating the particles for $x_{10}$ using $p(x_{10})$, which will can be arbitrary, but will be considered Gaussian. Initialize the weights for each particle to $1/N$, where $N$ is the number of particles. The Kalman filters are initialized with $x_{20}$ and $\boldsymbol{P}_{20}$. For each instance of time perform the following steps.

1. Update the weight for each particle

$$w_k^{i+1} = w_k^{(j)} exp\left[-\frac{1}{2}(\widetilde{\boldsymbol{y}}_k - \boldsymbol{y}_k^{(j)})R_k^{-1}(\widetilde{\boldsymbol{y}}_k - \boldsymbol{y}_k^{(j)})^T\right] \tag{F.8}$$

2. Re-normalize the weights

$$w_{k+1}^{(j)} \leftarrow \frac{w_{k+1}^{(j)}}{\sum_{j=1}^{N} w_{k+1}^{(j)}} \tag{F.9}$$

3. If needed, resample the weights

$$\boldsymbol{x}_{2k+1} = \boldsymbol{\Phi}_{2k}\boldsymbol{x}_{2k} + \boldsymbol{\Upsilon}_{2k}\boldsymbol{w}_{2k} \tag{F.10}$$

$$\widetilde{\boldsymbol{y}}_k = \boldsymbol{h}(\boldsymbol{x}_{1k}) + \boldsymbol{v}_k \tag{F.11}$$

4. Propagate the particles

$$\boldsymbol{x}_{1k+1} \sim N\left(f(\boldsymbol{x}_{1k}^{(j)}) + \boldsymbol{\Phi}_{1k}\boldsymbol{x}_{2k}^{-(j)}, \boldsymbol{\Phi}_{1k}\boldsymbol{P}_{2k}\boldsymbol{\Phi}_{1k}^T + \boldsymbol{\Upsilon}_{1k}Q_{1k}\boldsymbol{\Upsilon}_{1k}^T\right) \tag{F.12}$$

5. Compute the Kalman gain

$$\boldsymbol{K}_k = \boldsymbol{P}_{2k}^{-}\boldsymbol{\Phi}_{1k}^T[\boldsymbol{\Phi}_{1k}\boldsymbol{P}_{2k}^{-}\boldsymbol{\Phi}_{1k}^T + \boldsymbol{\Upsilon}_{1k}Q_{1k}\boldsymbol{\Upsilon}_{1k}^T]^{-1} \tag{F.13}$$

6. Perform update of Kalman filter for each particle

$$\boldsymbol{x}_{2k}^{+(j)} = \boldsymbol{x}_{2k}^{-(j)} + \boldsymbol{K}_k[\boldsymbol{x}_{1k+1}^{(j)} - f(\boldsymbol{x}_{1k}^{(j)}) - \boldsymbol{\Phi}_{1k}\boldsymbol{x}_{2k}^{-(j)}] \tag{F.14}$$

$$\boldsymbol{P}_{2k}^{+} = [\boldsymbol{I} - \boldsymbol{K}_k\boldsymbol{\Phi}_{1k}]\boldsymbol{P}_{2k}^{-} \tag{F.15}$$

7. Propagate the Kalman filters for each particle

$$\boldsymbol{x}_{2k+1}^{-(j)} = D_k\boldsymbol{x}_{2k}^{-(j)} + \boldsymbol{C}_k[\boldsymbol{x}_{1k+1}^{(j)} - f(\boldsymbol{x}_{1k}^{(j)})] \tag{F.16}$$

$$\boldsymbol{P}_{2k+1}^{-} = D_k\boldsymbol{P}_{2k}^{-}D_k^T + \boldsymbol{\Upsilon}_{2k}\bar{Q}_{2k}\boldsymbol{\Upsilon}_{2k}^T \tag{F.17}$$

where

$$\bar{Q}_{2k} = Q_{2k} + Q_{12k}^T Q_{1k}^{-1} Q_{12k} \tag{F.18}$$

$$C_k = \boldsymbol{\Upsilon}_{2k}Q_{12k}^T Q_{1k}^{-1}(\boldsymbol{\Upsilon}_{1k}^T\boldsymbol{\Upsilon}_{1k})^{-1}\boldsymbol{\Upsilon}_{1k}^T \tag{F.19}$$

$$D_k = \mathbf{\Phi}_{2k} - C_k\mathbf{\Phi}_{1k} \qquad\qquad (\text{F.20})$$

8. Vehicle state and covariance at each time step are calculated

$$\hat{\boldsymbol{x}}_k = \sum_{j=1}^{N} w_k^{(j)} \boldsymbol{x}_k^{(j)} \qquad\qquad (\text{F.21})$$

$$\boldsymbol{P}_k \approx \begin{bmatrix} 0_{n1\times n1} & 0_{n1\times n2} \\ 0_{n2\times n1} & P_{2k}^+ \end{bmatrix} + \sum_{j=1}^{N} w_k^{(j)} \tilde{\boldsymbol{x}}_k^{(j)} \tilde{\boldsymbol{x}}_k^{(j)T} \qquad\qquad (\text{F.22})$$

$$\tilde{\boldsymbol{x}}_k^{(j)} = \boldsymbol{x}_k^{(j)} - \hat{\boldsymbol{x}}_k \qquad\qquad (\text{F.23})$$

where $\boldsymbol{x}_k^{(j)} = \begin{bmatrix} \boldsymbol{x}_{1k}^{(j)T} & \boldsymbol{x}_2^{+(j)T} \end{bmatrix}^T$ and $n1$ and $n2$ are the lengths of $\boldsymbol{x}_1$ and $\boldsymbol{x}_2$

respectively. Since the process noise for $Q_{1k}$ and $Q_{12k}$ are zero, this reduces the above

equations where these variables are called out.

REFERENCES

[1] Kalman, R.E. (1960).  A New Approach to Linear Filtering and Prediction Problems, *Transactions of the ASME - Journal of Basic Engineering, 82 (Series D)*: 35-45. http://www.cs.unc.edu/~welch/kalman/media/pdf/Kalman1960.pdf

[2] McGee, L.A. & Schmidt, S.F. (1985). *Discovery of the Kalman Filter as a Practical Tool for Aerospace and Industry*.  (NASA-TM-86847).  National Aeronautics and Space Administration.  (Retrieved March 12, 2018 from NASA Technical Reports Server,   https://ntrs.nasa.gov/archive/nasa/casi.ntrs.nasa.gov/19860003843.pdf)

[3] Apollo Navigation Working Group. (1965, September 1). *Apollo Navigation Ground and Onboard Capabilities.* (Technical Report No. 65-AN-2.0). National Aeronautics and Space Administration. (Retrieved March 12, 2018 from NASA Technical Reports Server, https://ntrs.nasa.gov/archive/nasa/casi.ntrs.nasa.gov/19690020854.pdf)

[4] Julier, S.J., Uhlmann, J.K. & Durrant-Whyte, H.F. (1995, June). *A New Approach for Filtering Nonlinear Systems.* Proceedings of the American Control Conference, Seattle, WA.

[5] Crassidis, J.L. & Junkins, J.L. (2012). *Optimal Estimation of Dynamic Systems* (2nd ed.).  Boca Raton, FL: CRC Press.

[6] Vallado, D.A. (2004).  *Fundamentals of Astrodynamics and Applications* (2nd ed.).  El Segundo, CA: Microcosm Press.

[7] Battin, R.H. (1999).  *An Introduction to the Mathematics and Methods of Astrodynamics, Revised Edition.*  Reston, VA: American Institute of Aeronautics and Astronautics.

[8] Bate, R.R., Mueller, D.D. & White, J.E. (1971). Fundamentals of Astrodynamics. New York, NY: Dover Publications.

[9]  Crassidis, J.L. & Markley, F.L. (2003, July).  Unscented Filtering for Spacecraft Attitude Estimation, *Journal of Guidance Control and Dynamics*. *Vol. 26*: 536-542.

[10]  Nordland, J. & Gustafsson, F. (2001, June).  Sequential Monte Carlo Filtering Techniques Applied to Integrated Navigation Systems, *Proceedings of the 2001 American Control Conference, Vol. 6*: 4375 - 4380.

[11]  (2018). The Astronomical Almanac for the Year.  Washington, London: US GPO; HMSO.

[12]  Klein, I. & Filin, S. (2011, August). Lidar and INS Fusion in Periods of GPS Outages for Mobile Laser Scanning Mapping Systems, *Proceedings from International Society for Photogrammetry and Remote Sensing Calgary 2011 Workshop, Volume XXXVIII-5/W12:* 231-236.

[13]  Christian, J.A. & Lightsey, E.G.  (2009, September).  Review of Options for Autonomous Cislunar Navigation, *Journal   of Spacecraft and Rockets. Vol. 45, No. 5*: 1023-1036.

[14]  Christian, J.A. & Lightsey, E.G.  (2010).  Integrated Performance of an Autonomous Optical Navigation System for Space Exploration, *AIAA SPACE 2010 Conference & Exposition*, AIAA SPACE Forum.

BIOGRAPHICAL INFORMATION

Matthew Shaver received his Bachelor's of Science in Aerospace Engineering from North Carolina State University in 1998.  From 1998 to 2000, he served in the United States Air Force.  In 2000, he started working at Johnson Space Center in Houston, TX as navigation flight controller for the Space Shuttle.  After the end of the Space Shuttle program in 2011, he worked in the oil and gas industry and started work on his Master's of Science in Aerospace Engineering from the University of Texas at Arlington in 2012.  In 2013, he returned to JSC working for the ISS program as a flight controller working with visiting vehicle rendezvous and departure operations eventually moving to the engineering directorate to work on visiting vehicle integration to the ISS.